

©2013 Bibek Raman Parajuli

Report Documentation Page		Form Approved OMB No. 0704-0188
Public reporting burden for the collection of information is estimated to average 1 hour per response, including the time for reviewing instructions, searching existing data sources, gathering and maintaining the data needed, and completing and reviewing the collection of information. Send comments regarding this burden estimate or any other aspect of this collection of information, including suggestions for reducing this burden, to Washington Headquarters Services, Directorate for Information Operations and Reports, 1215 Jefferson Davis Highway, Suite 1204, Arlington VA 22202-4302. Respondents should be aware that notwithstanding any other provision of law, no person shall be subject to a penalty for failing to comply with a collection of information if it does not display a currently valid OMB control number.		
1. REPORT DATE 2013	2. REPORT TYPE	3. DATES COVERED 00-00-2013 to 00-00-2013
4. TITLE AND SUBTITLE Guiding of Plasmons and Phonons in Complex Three Dimensional Structures		5a. CONTRACT NUMBER
		5b. GRANT NUMBER
		5c. PROGRAM ELEMENT NUMBER
6. AUTHOR(S)	5d. PROJECT NUMBER	
	5e. TASK NUMBER	
	5f. WORK UNIT NUMBER	
7. PERFORMING ORGANIZATION NAME(S) AND ADDRESS(ES) University of Illinois at Urbana-Champaign, Department of Materials Science and Engineering, Urbana, IL, 61801		8. PERFORMING ORGANIZATION REPORT NUMBER
9. SPONSORING/MONITORING AGENCY NAME(S) AND ADDRESS(ES)		10. SPONSOR/MONITOR'S ACRONYM(S)
		11. SPONSOR/MONITOR'S REPORT NUMBER(S)
12. DISTRIBUTION/AVAILABILITY STATEMENT Approved for public release; distribution unlimited		
13. SUPPLEMENTARY NOTES		

14. ABSTRACT

The demand for pathways to fabricate and methodologies to understand 3D structures with advanced functionalities has increased significantly over the last years. Materials exhibiting three-dimensional structure with characteristic length scales ranging from nanometers to micrometers have extraordinary potential for emerging optical and thermal applications and are of great current interest in providing new functionalities for a host of applications. The thesis is divided into two primary parts. The majority of the thesis is devoted to understanding light-matter interaction in a new class of devices termed Resonant Guided Wave Networks (RGWNs). We describe how the geometrical properties of the network of waveguides are tuned in conjunction with the materials properties to realize a collective optical response contrary to other dispersive photonic materials where the response is limited to its discrete elements. In particular, we demonstrate a simple and efficient fabrication of MIM based complex 3D structure that offers a novel approach to optical dispersion control based on resonant structures. This is followed by a description of experiments that probe the optical response of the structures. Of particular interest are surface electromagnetic modes known as surface plasmonpolaritons (SPPs). In the second part of this thesis, we report measurements and modeling of thermal conductivity in periodic three-dimensional dielectric nanostructures: silicon inverse opals. Such structures represent a three-dimensional 'phononic crystal' but affect heat flow instead of acoustics. The thermal conductivity of inverse opal films are relatively low, ~0.6-1.4 W/mK at 300 K which is due to macroscopic bending of heat flow lines in the structure. The corresponding material thermal conductivity is in the range 5-12 W/mK and has an anomalous ~ 1.8 T dependence at low temperatures, distinct from the typical ~ 3 T behavior of bulk polycrystalline silicon. Using phonon scattering theory, we show such dependence arising from coherent phonon reflections in the inter-grain region. This is consistent with an unconfirmed theory proposed in 1955. The low thermal conductivity is significant for applications in photonics where they imply the possibility of significant temperature rise even at relatively low optical absorption and in thermoelectrics, where they suggest the possibility of enhancement in the figure of merit for polysilicon-based devices.

15. SUBJECT TERMS

16. SECURITY CLASSIFICATION OF:

a. REPORT

unclassified

b. ABSTRACT

unclassified

c. THIS PAGE

unclassified17. LIMITATION OF
ABSTRACT**Same as
Report (SAR)**18. NUMBER
OF PAGES**80**19a. NAME OF
RESPONSIBLE PERSON

GUIDING OF PLASMONS AND PHONONS IN COMPLEX
THREE DIMENSIONAL STRUCTURES

BY

BIBEK RAMAN PARAJULI

THESIS

Submitted in partial fulfillment of the requirements
for the degree of Master of Science in Materials Science and Engineering
in the Graduate College of the
University of Illinois at Urbana-Champaign, 2013

Urbana, Illinois

Adviser:

Professor Paul V. Braun

ABSTRACT

The demand for pathways to fabricate and methodologies to understand 3D structures with advanced functionalities has increased significantly over the last years. Materials exhibiting three-dimensional structure with characteristic length scales ranging from nanometers to micrometers have extraordinary potential for emerging optical and thermal applications and are of great current interest in providing new functionalities for a host of applications.

The thesis is divided into two primary parts. The majority of the thesis is devoted to understanding light-matter interaction in a new class of devices termed Resonant Guided Wave Networks (RGWNs). We describe how the geometrical properties of the network of waveguides are tuned in conjunction with the materials properties to realize a collective optical response, contrary to other dispersive photonic materials where the response is limited to its discrete elements. In particular, we demonstrate a simple and efficient fabrication of MIM based complex 3D structure that offers a novel approach to optical dispersion control based on resonant structures. This is followed by a description of experiments that probe the optical response of the structures. Of particular interest are surface electromagnetic modes known as surface plasmon-polaritons (SPPs).

In the second part of this thesis, we report measurements and modeling of thermal conductivity in periodic three-dimensional dielectric nanostructures: silicon inverse opals. Such structures represent a three-dimensional “phononic crystal” but affect heat flow instead of acoustics. The thermal conductivity of inverse opal films are relatively low, $\sim 0.6\text{-}1.4$ W/mK at 300 K which is due to macroscopic bending of heat flow lines in the structure. The corresponding material thermal conductivity is in the range 5-12 W/mK and has an anomalous $\sim T^{1.8}$ dependence at low temperatures, distinct from the typical $\sim T^3$ behavior of bulk polycrystalline silicon. Using phonon scattering theory, we show such dependence arising from coherent phonon reflections in the inter-grain region. This is consistent with an unconfirmed theory proposed in 1955. The low thermal conductivity is significant for applications in photonics where they imply the possibility of significant temperature rise even at relatively low optical absorption and in thermoelectrics, where they suggest the possibility of enhancement in the figure of merit for polysilicon-based devices.

ACKNOWLEDGEMENTS

It is my great pleasure to thank everyone who has helped in making this work possible. First and foremost, I am sincerely thankful to my adviser, Professor Paul V. Braun, for his guidance and support throughout my research. He has been an amazing mentor with unending source of ideas and always took time to patiently discuss every detail of the work. I really appreciate his endless support, positive attitude, availability, and his commitment to education. I will forever be grateful for what I have learned from him.

My colleagues have been a source of immense support during this work. I would specially like to thank Dr. Agustin Mihi, Dr. Huigang Zhang, Dr. Jiung Cho, Dr. Ming Fu, and Dr. Kevin Arpin for their guidance, availability, advice and helpful discussion at all times. Next, I would like to thank fellow Braun group members Matthew Goodman, Hailong Ning, Neil Krueger, Chunjie Zhang, and Junjie Wang for their insightful research discussions, experimental assistance and making lab atmosphere enjoyable, filled with laughter and memories.

This work would not be possible without the help from my collaborators Stanley Burgos, Bok Y. Ahn, and Jun Ma. I am fortunate to have Stanley as a collaborator as he was an excellent mentor of plasmonics and EM theory during my first year as a graduate student. I would also like to thank Erica Malloch, Michelle Lynn Malloch, and Jay Menacher for their administrative support and availability.

I would like to thank the facilities and staff members at the Materials Research Laboratory (MRL) and Beckman Institute at the University of Illinois at Urbana-Champaign. Their contribution to this work is truly invaluable. I'd also like to acknowledge the funding sources that made thesis research possible, including grants from Light-Material Interaction in Energy Conversion- Energy Frontier Research Center (LMI-EFRC) and Air Force Office of Scientific Research (AFOSR).

Finally, this work would not be possible without the support and encouragement of my family and friends. Words cannot express my gratitude for my family's unconditional love and support. I have had the opportunity to meet great people during my stay at Urbana-Champaign. I am grateful for their honest opinions, support and encouragement throughout these years. They added great memories to my graduate college experience that I will always cherish.

TABLE OF CONTENTS

PART I PLASMONS IN COMPLEX 3D-STRUCTURE (RGWNS)	1
CHAPTER 1 INTRODUCTION TO SURFACE PLASMONS	2
1.1 Light-matter interaction.....	2
1.2 Optical properties of metals	3
1.3 Surface Plasmon Polaritons (SPPs).....	5
1.3.1 Literature review.....	5
1.3.2 Properties of SPPs	6
1.3.3 Dispersion relation	8
1.3.4 Propagation length and skin depth	9
1.4 Metal-Insulator-Metal (MIM) waveguide.....	9
CHAPTER 2 RESONANT GUIDED WAVE NETWORKS (RGWNS).....	11
2.1 Dispersive photonic materials	11
2.2 Resonant Guided Wave Networks (RGWNs).....	13
2.3 Fabrication process.....	15
2.3.1 Direct-ink writing.....	15
2.3.2 Thermal stability of the direct-written structure.....	18
2.3.3 Choice of metal	19
2.3.4 Electrodeposition of silver	19
2.3.5 Electropolishing of silver.....	22
2.3.6 Thermal annealing and its effect on the silver coating.....	24
2.3.7 Chemical Vapor Deposition (CVD) of silicon	26
2.3.8 Electroless plating of silver	27
2.4 Final structure.....	30
CHAPTER 3 OPTICAL CHARACTERIZATION OF 3D RGWNS.....	32
3.1 Introduction	32
3.2 Optical response of the silver coating (optimized).....	33
3.3 Experimental realization	34
3.3.1 FIB to open the structure	34
3.3.2 Angle-resolved Fourier Spectroscopy.....	36

CHAPTER 4 CONCLUSION AND FUTURE OUTLOOK.....	40
4.1 Conclusion.....	40
4.2 Future outlook	42
4.2.1 <i>Fabrication</i>	42
4.2.2 <i>Characterization</i>	44
 PART II PHONON TRANSPORT IN COMPLEX 3D-STRUCTURE (SILICON INVERSE OPALS)	45
CHAPTER 5 COHERENT PHONON-GRAIN BOUNDARY SCATTERING IN SILICON INVERSE OPALS	46
5.1 Background and general concepts.....	46
5.2 Fabrication of silicon inverse structures.....	49
5.3 Shell thickness and grain size characterization.....	51
5.4 Thermal conductivity measurements	53
5.4.1 <i>The 3ω method</i>	53
5.4.2 <i>Data and discussion</i>	54
5.4.3 <i>Phonon-grain boundary scattering theory</i>	58
5.4.4 <i>Thermal conductivity modeling</i>	60
5.5 Results and discussion.....	61
5.6 Conclusion.....	64
 REFERENCES	66

PART I

PLASMONS IN COMPLEX 3D-STRUCTURE (RGWNs)*

*This work was done in collaboration with Stanley Burgos from Atwater Research group at Caltech and Bok Y. Ahn from Lewis Research Group at School of Engineering and Applied Sciences, Harvard.

CHAPTER 1

INTRODUCTION TO SURFACE PLASMONS

1.1 Light-matter interaction

Light-matter interactions have fascinated mankind for thousands of years, and are the basis of some of the most famous scientific discoveries to date. With the continued miniaturization and integration of photonic circuits, recent advances are becoming greatly limited by diffraction. In classical optics, diffraction restricts the localization of electromagnetic waves into nanoscale regions much smaller than the wavelength of light in the material¹. However, the electromagnetic response of metals has led to the development of the emerging and fast growing research field of plasmonics. Plasmonics opens a path for controlling light-matter interactions on the subwavelength scale, serving as a bridge between diffraction-limited optics and nanoscale devices².

The strong interaction between light and metal has been exploited for thousands of years, most recognizably in the art of creating brightly colored stained-glass window panels (**Figure 1.1a**) by introducing metallic salts in otherwise transparent glass matrix. One of the famous example is the “Lycurgus Cup”³ dating back to the 4th century Rome (**Figure 1.1b**). Viewed normally by reflected light the surface is opaque olive green, but when backlit the cup is a brilliant translucent red. This fascinating observation is due to the inclusion of gold and silver particles within the glass matrix, which strongly scatter green light but transmit red.

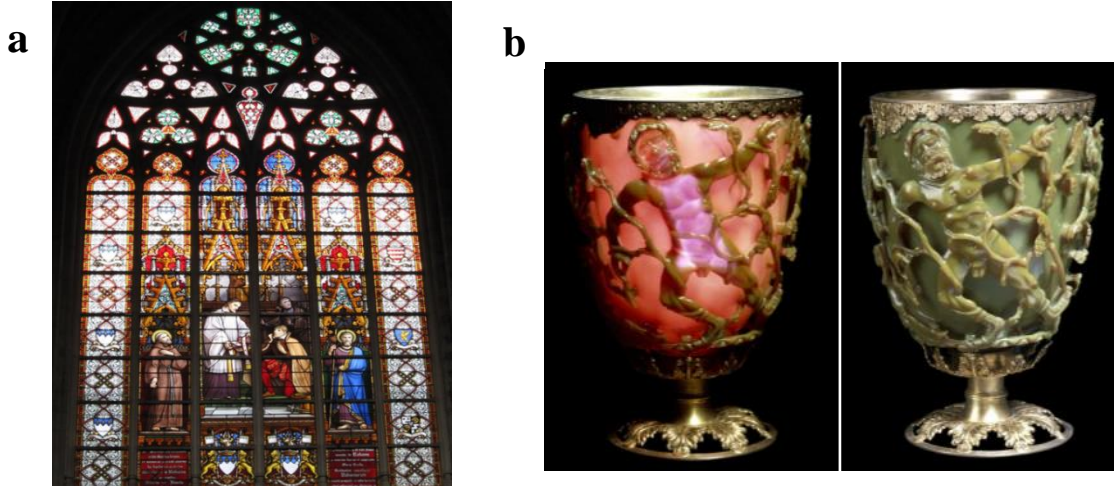


Figure 1.1 – (a) Stained glass window in Rome with its brilliant colors. (b) The Lycurgus cup from 4th century Rome. The glass consists of silver and gold nanoparticles. Image reproduced from Reference 3.

Fundamental research and development of metal based structures and devices have attracted a number of groups in recent years to manipulate light at length scales smaller than the wavelength of light by employing surface plasmons at metal-air and metal-dielectric interfaces. In this chapter, I review the electromagnetic properties of metals in the optical frequency regime. An exploration into light-metal interactions will then be presented, building up to studying the properties of surface plasmons in order to understand how they can be employed to control and manipulate light at the metal-dielectric interface.

1.2 Optical properties of metals

Metals constitute majority of the periodic table and have been studied for thousands of years. In the most simple description, metals can be thought of as a sea of free electrons oscillating within a lattice of fixed ion cores. These electrons are free to move throughout the metal and respond to any applied external field. However, the electron's response to an optical field is entirely dependent on the frequency response of the metal's dielectric constant⁴.

By using the Drude model for metals, one can obtain the dielectric constant of metals as a function of frequency in the following form

$$\epsilon(\omega) = 1 - \frac{\omega_p^2}{\omega^2 \left(\frac{i}{\omega\tau} + 1 \right)} \quad (1)$$

where ω_p is the plasmon frequency of the corresponding bulk metal, and τ is the electron relaxation time in that metal. When one neglects the collision (lossless i.e. $\omega \gg \tau$), we get

$$\epsilon(\omega) = 1 - \frac{\omega_p^2}{\omega^2} \quad (2)$$

Therefore, metals have negative dielectric constants at frequencies smaller than plasma frequency.

At low (microwave and far-infrared) frequencies, many metals behave like a perfect electrical conductor with high reflectivities and negligible electromagnetic field penetration. Hence, metals are not the first materials that come to mind for designing optical elements. However, above certain frequency, the driving field strongly couples into the longitudinal oscillations of the bulk electrons within the metal⁴. This is known as the plasma frequency of the metal and is given by

$$\omega_p = \sqrt{\frac{4\pi n e^2}{m^*}} \quad (3)$$

where n is the density of electrons within the metal and m^* is the effective mass of the electrons.

For noble metals of interest like gold, silver, and copper, the optical frequency regime lies below their plasma frequency giving them a negative dielectric constant as can be seen from **Equation 2**. When such metals meet another material with a positive permittivity, an electromagnetic wave can be bounded by their interface according to the Maxwell equations⁵.

1.3 Surface Plasmon Polaritons (SPPs)

As discussed in the previous section, the negative dielectric constant of metals at optical frequencies leads to existence of longitudinal charge-density fluctuations along a metal-dielectric interface. These coherent oscillations of free electrons are referred to as surface plasmons (SPs)⁶. SPs can couple with electromagnetic waves resulting in a freely propagating surface plasmon polaritons (SPPs)⁷ along metal surfaces to localized surface plasmons⁸ on metallic nanoparticles (**Figure 1.2**). Propagating SPPs allows significant reduction in effective wavelength and a corresponding significant increase in spatial confinement and local field intensity, and will be the focus of this thesis.

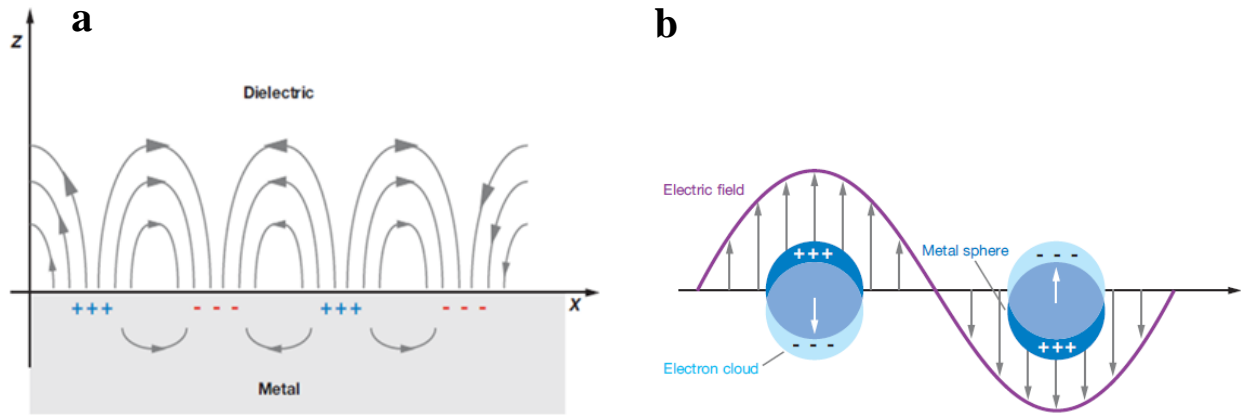


Figure 1.2 – Schematic diagrams illustrating the charge and electric field associated with (a) a propagating surface plasmon on an extended metal film and (b) a localized surface plasmon on a metal nano-particle. Image reproduced from Reference 7.

1.3.1 Literature review

The first scientific observation of surface plasmons date back to 1902 by Robert W. Wood⁹. In 1904, J.C.M. Garnett first describes the bright colors observed in metal doped glasses¹⁰ employing the contemporary Drude model of free-electron metals and the electromagnetic properties of small spheres as derived by Lord Rayleigh¹¹. Shortly thereafter, in

1908, Gustav Mie presented a general formulation for the scattering of light from spherical surfaces, including the particular case of colloidal nanoparticles of varying size¹². The theoretical description of surface plasmons on thin films was first described in terms of electron energy loss spectroscopy measurements in 1957, by Ritchie¹³. In 1968, nearly seventy years after Wood's original observations, Ritchie and coworkers describe the anomalous behavior of metal gratings in terms of surface plasmon resonances excited on the gratings¹⁴.

A major experimental milestone in the study of surface plasmons was made in 1968 when Andreas Otto¹⁵ as well as Erich Kretschmann and Heinz Raether¹⁶ developed methods for the optical excitation of surface plasmons on metal films, making experiments on surface plasmons easily accessible to many researchers. As the field continued to develop, and the importance of the coupling between the oscillating electrons and the electromagnetic field become more apparent, Stephen Cunningham and his colleagues coined the term “surface plasmon- polariton” (SPP) in 1974¹⁷. All these findings have set the stage for the current surge in surface plasmon research in recent years.

1.3.2 Properties of SPPs

The electric field associated with SPPs is strongly confined (sub-wavelength) and decays exponentially with increasing distance from the interface (**Figure 1.3a**)⁴. Many of the appealing features of SPPs come from this confinement: The electric field strength in the vicinity of the interface is enhanced, providing possibilities to enable a wide range of practical applications including light guiding and manipulation at nanoscale¹⁸⁻²², biodetection at single molecule level²³⁻²⁵, enhanced optical transmission through subwavelength apertures^{26,27}, high resolution optical imaging below the diffraction limit²⁸⁻³⁰, and solar cells^{31,32}. Recently, considerable focus

has been directed to exploit the dispersion characteristics of SPPs traveling in confined metallo-dielectric spaces^{33,34} to create photonic materials with artificially tailored bulk optical properties, which will be the focus of this thesis.

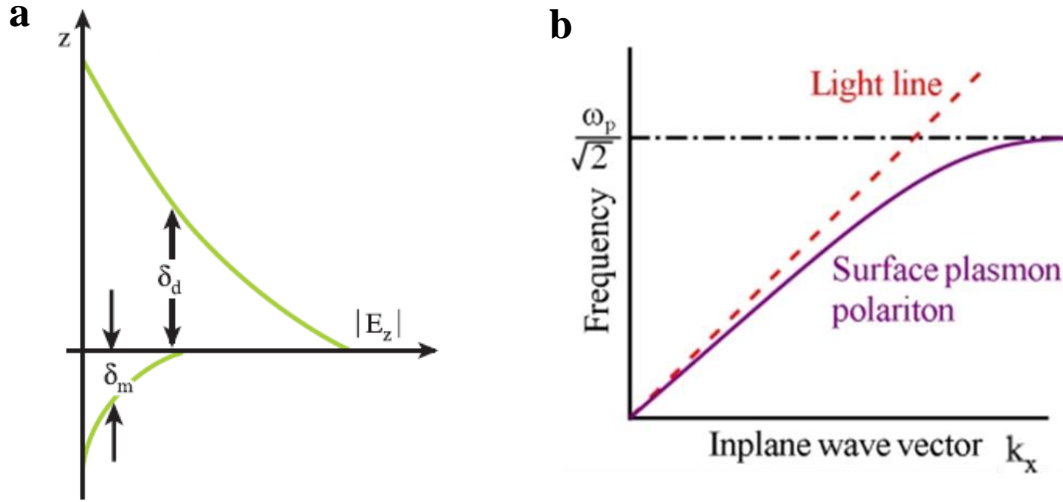


Figure 1.3 – (a) Electric field distribution perpendicular to the surface. The SPP electromagnetic field decays exponentially with increasing distance into each medium from the interface. (b) Dispersion relation for a surface plasmon, light line represents dispersion for light in a vacuum.

The short-wavelength SPPs enable the fabrication of nanoscale optical integrated circuits, in which light can be guided, split, filtered, and even amplified using plasmonic integrated circuits that are smaller than the optical wavelength. Since photons can be coupled to plasmons and vice versa and the frequency range of SPPs extends over the infrared and visible spectrum, they also provide a new platform for optical communication³⁵. However, their decay due to both scattering from the surface imperfections and ohmic losses within the metal has limited their application. With the advances in micro-nano fabrication technologies, there has been significant improvement in SPP properties particularly the choice of metal (dispersion), metal thickness, and excitation frequency³⁶.

1.3.3 Dispersion relation

The electromagnetic field associated with SPP at a dielectric/metal interface can be obtained by solving Maxwell's equations⁴. From the solution one obtains SPP's dispersion relation, that is, the SPP energy (or frequency) as a function of its wave-vector (**Figure 1.3b**),

$$k_{SPP} = \frac{\omega}{c} \sqrt{\frac{\epsilon_d \epsilon_m}{\epsilon_d + \epsilon_m}} = k_x' + i k_x'' \quad (4)$$

where ϵ_d and ϵ_m are the frequency dependent dielectric function of the dielectric and metal respectively.

The SPP dispersion relation, $\omega(k)$ plotted in **Figure 1.3b**, shows that for small wave vectors the plasmon is close to that of the light line, but always to the right hand side. Therefore, the plasmon has similar properties to the optical field but always has a greater momentum and is non-radiative. This increased momentum is associated with the binding of the mode to the surface. For larger wave vectors the surface plasmon dispersion tends towards a maximum value of $\omega_p/\sqrt{2}$, and resembles that of the bulk plasmon and is radiative, the energy becoming independent of wave vector.

Since SPPs do not directly couple to an optical field they must be created via some intermediate step¹. This requires either converting the incident light into an evanescent mode by means of total internal reflection, or by scattering the light to higher momentum via a grating or scattering site. Basically, some mechanism must be introduced to effectively increase the wave vector of the incident light in order to achieve momentum matching between the surface plasmons and the free-space photons at a given energy as evident from **Figure 1.3b**. While discussing the dispersion relation it is of worth to discuss the spatial extent of the fields associated with the SPP mode.

1.3.4 Propagation length and skin depth

Due to the imaginary part of ϵ_m , the propagation distance of SPPs is limited due to absorption in the metal. The finite propagation length is accounted for by the imaginary part of k_{SPP} . As the SPP mode propagates, the electric field amplitude decays exponentially as $\exp(-k''_x x)$ and therefore the intensity as $\exp(-2k''_x x)$. We can define the propagation distance L as the $1/e$ decay length of the field intensity along x ,

$$L = \frac{1}{2k''_x} \approx \frac{c}{\omega} \left(\frac{\epsilon_d + \epsilon'_m}{\epsilon_d \epsilon'_m} \right)^{3/2} \frac{(\epsilon'_m)^2}{\epsilon''_m} \quad (5)$$

Here ϵ'_m and ϵ''_m are the real and imaginary parts of the dielectric function of the metal such that $\epsilon_m = \epsilon'_m + i\epsilon''_m$.

The propagation distance depends on the dielectric constant of the metal and the operating frequency ranging from 10 μm in the visible to millimeter in the infrared for metals with low adsorption loss such as silver, gold⁴. The field penetration (plasmon skin depth) within the dielectric and the metal are of the order of tens to hundreds of nm as shown in **Figure 1.3a**.

1.4 Metal-Insulator-Metal (MIM) waveguide

As mentioned earlier, surface plasmons on a planar metal-dielectric interface allow significant reduction in the effective wavelength and a corresponding significant increase in spatial confinement and local field intensity of the light. Placing a second metal layer above the dielectric, one can achieve a metal-insulator-metal (MIM) waveguide with extremely high modal confinement³⁷ as shown in **Figure 1.4**. This significantly reduces the decay of optical field by confining the electromagnetic field in the dielectric region.

Provided the thickness of the metal film exceeds the plasmon skin depth, oscillations at each metal-dielectric interface are decoupled, and independent surface plasmon modes at each metal-dielectric interface are sustained.

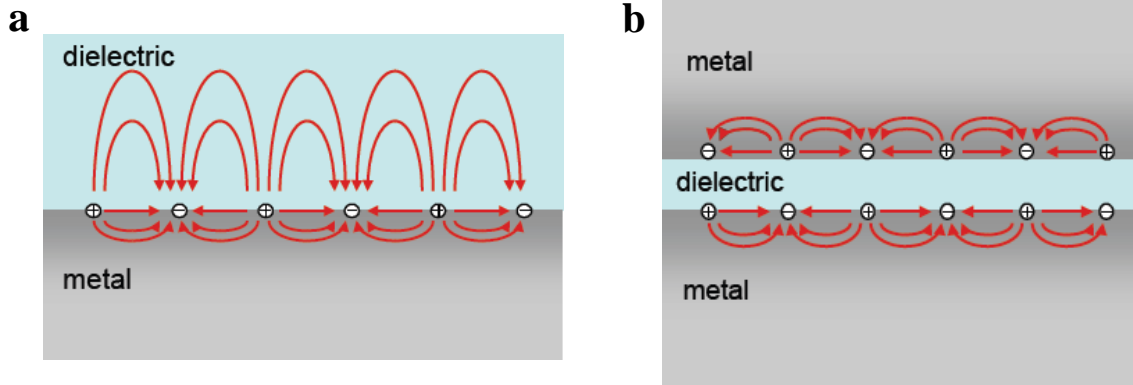


Figure 1.4 – Schematic showing the electric field lines of a surface plasmon **(a)** at a metal-dielectric interface, and **(b)** for a metal-insulator-metal waveguide. Image reproduced from Reference 37.

As seen in **Figure 1.4**, the MIM geometry significantly confines the electromagnetic fields in the dielectric region more than a single metallodielectric interface. By using dielectrics with higher refractive index, one can decrease the element size of the plasmonic device to the nanometer scale by localizing light within thinner insulator thickness. In addition, the output of the device can be tuned across the visible and infrared region of the electromagnetic spectrum by replacing the insulator layer with an active material. By changing each of the materials in the three layer stack (**Figure 1.4b**), as well as their relative thicknesses, the dispersion properties of the device as well as the resonance and filtering properties can be tuned over a wide range of the electromagnetic spectrum. In addition, by changing the dimensions of the structures, as well as the distance between them, we can selectively access a large range of k -vectors or wavelengths that are present within the structure.

CHAPTER 2

RESONANT GUIDED WAVE NETWORKS (RGWNS)

2.1 Dispersive photonic materials

Nanofabricated systems that exploit SPPs demonstrate potential for controlling light-matter interaction on subwavelength scale, enabling nanophotonic technologies that are unattainable with conventional diffraction-limited optical systems². SPPs are able to channel light efficiently into nanometer scale volumes, leading to direct modification of resonance frequency dispersion properties (substantially shrinking the wavelength and speed of light for example), as well as field enhancements suitable for enabling strong nonlinear effects⁴. In this thesis, we introduce a novel approach to optical dispersion control based on three-dimensional (3D) metallo-dielectric periodic structures by exploiting the dispersion characteristics of SPPs. Materials exhibiting three-dimensional structure with characteristic lengths ranging from nanometers to micrometers have extraordinary potential for emerging optical applications based on the regulation of light-matter interactions via the local interaction of periodic elements. The majority of this chapter is focused on the design, fabrication, and experimental characterization of these resonant based plasmonic structures.

Recent years have seen a rapid growth of research into various artificial photonic material concepts that have defined new directions to control optical dispersion, thus exhibiting superior electromagnetic properties. Most of the work has been dedicated to metamaterials due to their new and seemingly exotic electromagnetic response. Metamaterials are artificially engineered metallo-dielectric structures patterned to sizes much smaller than the operating wavelength, and their special geometrical arrangement affects the permittivity and permeability of the

electromagnetic field to achieve light propagation and manipulation different than their constituent materials, in a way not achievable through natural medium^{18,38,39}. These engineered metamaterials enable a host of novel effects such as negative index of refraction, optical cloaking, and sub-diffraction imaging. They commonly require complex multidimensional building blocks, which are difficult, if not impossible, to achieve via standard technology. Also, use of metals at higher frequency can be problematic due to their losses. As an alternative, researchers investigated into periodic structures typically composed of low loss dielectrics known as photonic crystals (PCs). PCs offer unprecedented control of light propagation in a way similar to how the periodicity of crystals effect the motion of electrons by defining allowed and forbidden energy bands^{40,41}. PCs are the optical analogs to semiconductors that have gained a lot of interest especially due to their ability to suppress light propagation in all three dimensions (complete photonic band gap)⁴². In other words, PCs provide a platform to engineer light-matter interaction at will. Another novel approach to light manipulation utilizes high Q optical resonators that are kept in close proximity to one another. The resonators are based on whispery gallery modes and are able to manipulate light propagation through evanescent coupling of the electromagnetic field⁴³.

In this chapter, I will focus on a fairly new approach for optical dispersion control based on resonant guided network of MIM waveguides. These structures were recently proposed and are referred to as resonant guided wave networks (RGWNs)⁴⁴.

2.2 Resonant Guided Wave Networks (RGWNs)

RGWNs offer a novel approach to optical dispersion control based on localized resonance within these structures⁴⁴. RGWNs are normally intersecting MIM waveguides that serve as wave splitting elements arranged in two- or three-dimensional networks (**Figure 2.1a**). The resulting network resonances give rise to wave dispersion that is sensitive to the network layout, contrary to other dispersive photonic systems. RWGNs have demonstrated potential for highly efficient resonators, band-gap materials⁴⁴ and devices with programmable optical transmission properties⁴⁵.

We will first introduce the properties of RGWN building block and investigate the wave dynamics within these structures using the finite-difference time-domain (FDTD) method with a short pulse excitation at a central wavelength of 1.5 μm . A resonant guided wave network is comprised of power splitting elements connected by isolated waveguides (**Figure 2.1a**).

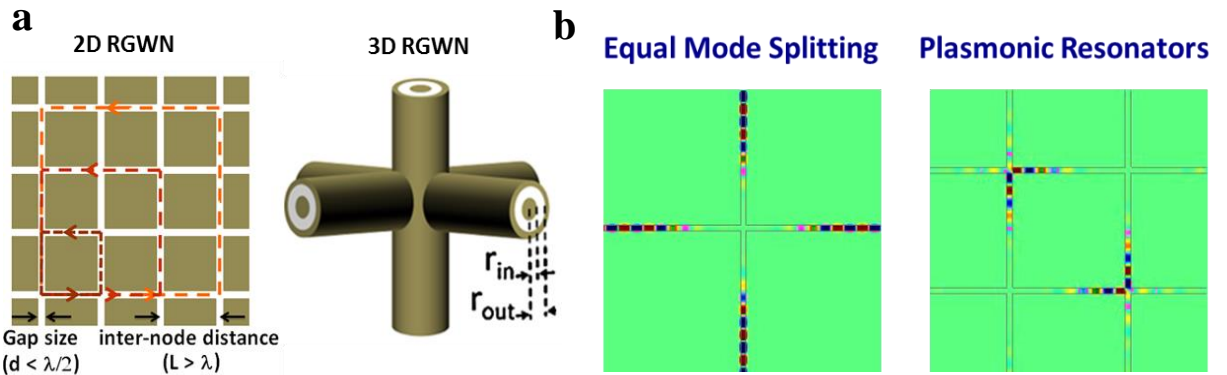


Figure 2.1 – (a) Schematic of RGWN building block. (b) Equal mode splitting in RGWNs (left); RGWNs as optical resonators (right). Image reproduced from Reference 44.

The power splitting elements distribute the incoming pulse to the waveguides connected to the junction with certain phase and amplitude. It was recently found that a cross junction of two normally intersecting MIM waveguides exhibit equal splitting of optical power at

subwavelength gap sizes⁴⁶. The subwavelength MIM junction serves as a nano-aperture (scattering site) for the incoming pulse, resulting in a broad spectrum of plane waves with significant fraction of the optical power coupling into the waveguides perpendicular to the input waveguide. This strong coupling of the incoming pulse to all neighboring waveguides gives this structure an optical response different from purely dielectric waveguides, where most of the power is transmitted in the forward direction. The nano-aperture effect is limited for dielectric waveguides by their half-wavelength modal cross-sections.

In addition to the equal-power splitting, the transmitted and the reflected pulses are out-of-phase. The pulses undergo interference inside the network, and interfere destructively or constructively depending on the waveguide length and network topology. Hence, if one appropriately designs the junction and waveguide components as well as the network layout with subwavelength gap size and internode distance on the order of the effective wavelength, a small 2 x 2 resonant-guided wave networks can function as an ultracompact optical resonator (**Figure 2.1b**). By controlling the properties of each splitting element and every waveguide, the network interference and resonances can be determined and thus also the optical function of the network⁴⁵. Also, the local network topology can be adjusted to operate the structure over broad range of frequencies.

Now if we consider an infinite 2D RGWN structure, photonic bandgaps are observed due to the interference effect as shown in **Figure 2.2a**. In other words, certain wavelength of light would enter a resonant state and not get transmitted, giving this structure a photonic bandgap. The photonic bandgap can be engineered by controlling the dispersion properties of the network: the phase-shift upon splitting which is controlled by the width of the MIM gaps and the interference which is dependent on the distance between the nodes.

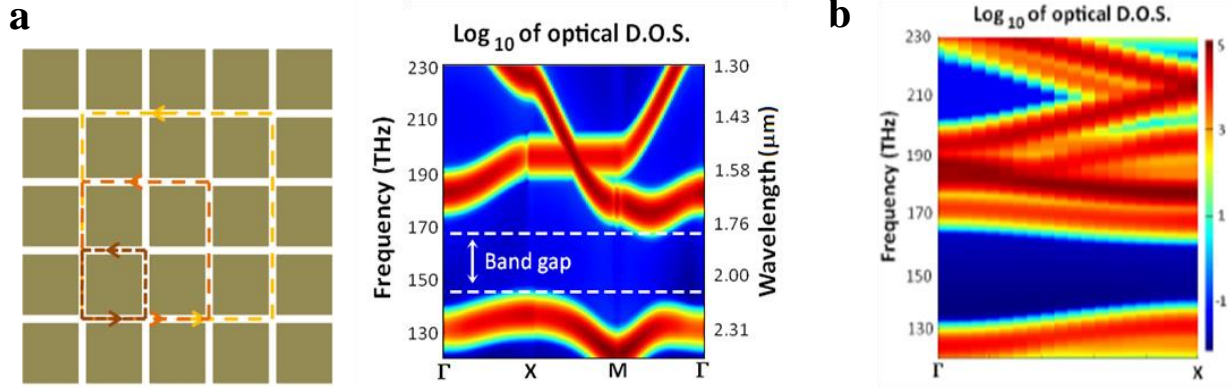


Figure 2.2 – (a) Optical density of states (right) for an infinite 2D RGWNs (left). (b) Optical density of an infinite 3D network. Image reproduced from Reference 44.

The wave dynamics is the same for 3D RGWNs, however, the four-arm cross junction element of the 2D network is replaced by a six arm cross junction in a 3D network (**Figure 2.1a**). It has been demonstrated that six-way equal power splitting occurs in the 3D coaxial MIM waveguide networks⁴⁴. Likewise the dispersion properties are governed by the local network topology giving the structure tunable photonic bandgap (**Figure 2.2b**).

2.3 Fabrication process

2.3.1 Direct-ink writing

The ability to pattern materials in three dimensions is critical for a number of emerging technologies, including photonics^{47,48}, microfluidics⁴⁹, microelectromechanical systems⁵⁰, biomaterials^{51,52}, batteries⁵³, and optoelectronics⁵⁴. I specifically have focused on direct-writing fabrication techniques,⁵⁵ which allows one to design and rapidly fabricate complex three-dimensional structures without the need for expensive and complicated tools, dies, or lithographic routes. In this method, a concentrated ink is extruded through a tapered cylindrical

nozzle that is translated onto the substrate using a computer-controlled 3-axis micropositioning stage (**Figure 2.3a**). Due to the viscoelastic ink characteristics, direct-ink writing enables self-supporting flexible, stretchable and spanning features from $0.1\mu\text{m}$ – $250\mu\text{m}$ ⁵⁵. This low-cost, large-area fabrication method with higher flexibility in material selection overcomes many challenges that exist with the pre-existing printing techniques for fabrication of complex 3D structure.

We use a direct-written 3D woodpile structure as a scaffold to fabricate the coaxial 3D RGWNs (**Figure 2.3b**). The scaffold is composed of highly concentrated silver nanoparticles ink with a solid loading of $\sim 80\%$ ⁵⁶. The scaffold network is coated with thin Ag film ($\sim 150\text{ nm}$) via electrodeposition, and then coated with silicon ($\sim 200\text{ nm}$) using Si-CVD followed by a second Ag electrodeposition. The thicknesses were appropriately chosen to ensure coherent plasmonic mode propagation and the resonant behavior using FDTD simulations. The schematic of the structure is shown below (**Figure 2.3c-d**).

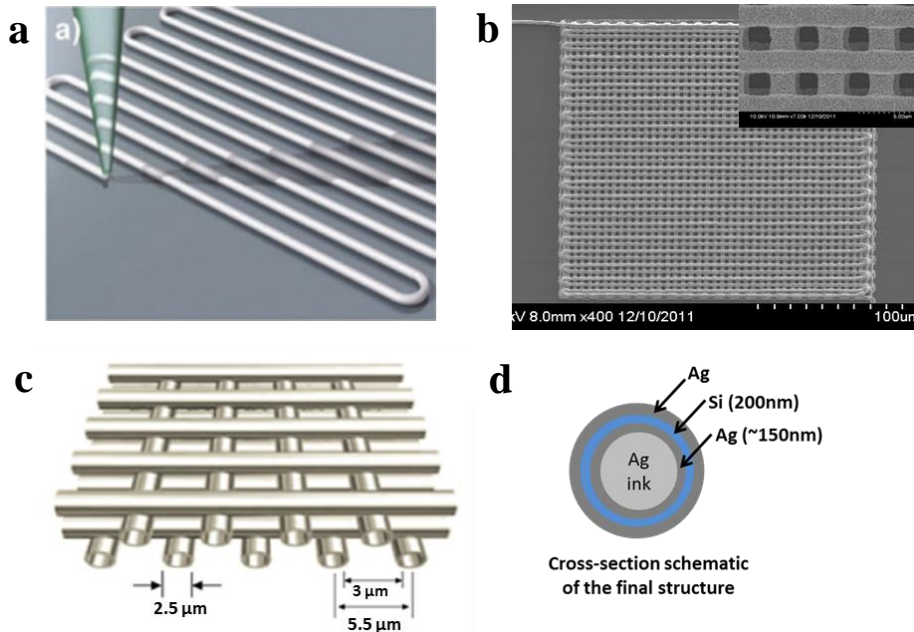


Figure 2.3 – (a) Schematic illustration of direct-write assembly. Image reproduced from Reference 56. (b) SEM image of the direct-written 3D woodpile scaffold. Inset shows the magnified view. (c) Schematic of the unit structure for 3D RGWN structure. (d) Schematic of the cross-section of the 3D RGWNs.

The 3D scaffold is composed of silver nanoparticles along with some polymer additive to promote uniform printing contrary to pure silver. This composite, particle-based structure is not ideal for plasmonic properties. Hence, we coat the structure with a thin conformal silver film. However, when printed, the silver nanoparticles are not yet bonded together, and thus thermal annealing, which allows removal of the organic additives to some extent and promote nanoparticle sintering, is performed before coating with a thin layer of conformal silver. The thermal treatment increases the electrical conductivity of the printed 3D scaffold⁵⁶. This is critical for the uniform and conformal electro-deposition of silver film. The conductivity of the ink as a function of annealing temperature is shown in **Figure 2.4**.

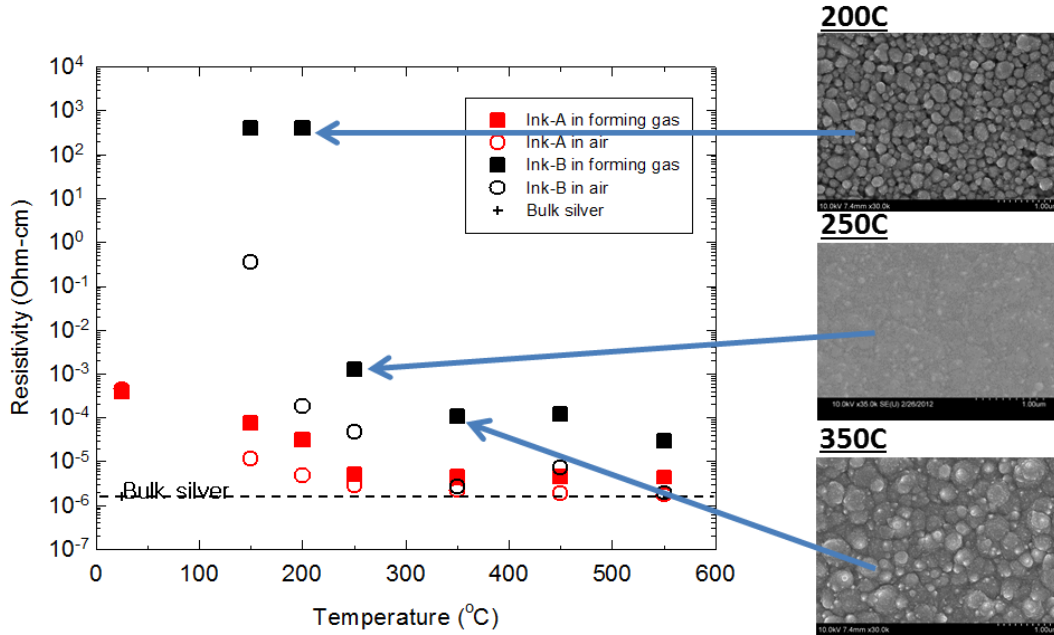


Figure 2.4 – Resistivity of direct-written silver ink films as a function of annealing temperature. Right shows top view SEM images of the silver coating on annealed silver ink films.

For annealing temperatures below 250 $^{\circ}\text{C}$, the conductivity of the silver ink is not high enough for silver deposition. However, at higher annealing temperatures the deposited silver gets rougher. As discussed in **Section 1.3**, surface plasmons are very sensitive to surface inhomogeneties as SPPs exist and propagate very close to the interface. Hence, optimizing the

surface roughness and other homogeneities is very critical while fabricating these structures as any inhomogeneities lead to scattering losses and limited propagation in addition to the intrinsic absorption loss from the metal. Also, the surface morphology of the electrodeposited silver determines the surface morphology of both the metal-dielectric interface, making surface roughness of electrodeposited silver particularly detrimental to device performance.

2.3.2 Thermal stability of the direct-written structure

Thermal annealing increases the mechanical stability of the structure which is critical during further processing at elevated temperatures. However, the silver scaffold suffers serious structural degradation due to grain growth and voids at high temperature and would often distort and delaminate from the substrate.

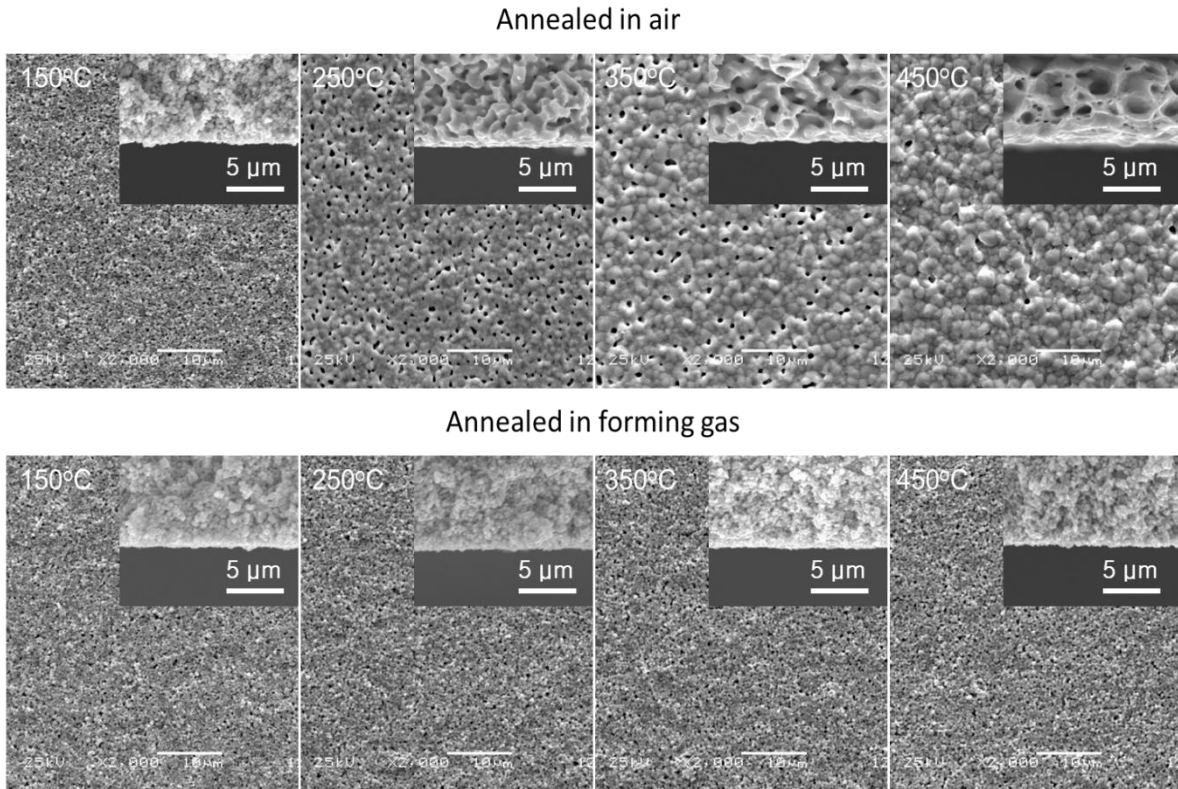


Figure 2.5 – Top view SEM images of silver ink films after annealing at different temperature. Inset shows the cross-section view. Top samples were annealed in air and bottom samples in forming gas.

We were able to achieve the structural integrity even at higher temperature by annealing the structure under forming gas (5% H_2 in Ar) as opposed to air⁵⁶ (**Figure 2.5**). The ideal annealing condition (250°C for 3 hrs, ramping rate 2°C/min⁻¹) was determined experimentally for optimized surface roughness of the electroplated silver (Section 2.3.4) on the printed 3D scaffold.

2.3.3 *Choice of metal*

As discussed earlier, metallic components are invariably accompanied by losses that can be detrimental to the SPPs properties thus limiting the feasibility of many novel plasmonic applications. Hence, the choice of metal is very critical while fabricating these plasmonic structures to achieve better device's performance. Owing to their relatively lower loss, noble metals such as gold, silver, and copper are conventionally used as metallic components at optical frequencies.

The SPP property is entirely dependent on the frequency response of the metal's dielectric constant. The real part of the dielectric function (ϵ'_m) describes the strength of the surface plasmons (polarization) induced by an external electric field, and the imaginary part (ϵ''_m) describes the losses encountered. The metal of choice is associated with large negative values of ϵ'_m and small values of ϵ''_m . Hence, silver is the metal of choice for plasmonics in the near-infrared region⁵⁷.

2.3.4 *Electrodeposition of silver*

After the annealing condition was optimized @ 250C for 3 hrs, the 3D woodpile scaffold was coated with a very thin, conformal silver film via electroplating. Electroplating is a process

in which metal ions in a solution are moved by an electric field from anode to coat an object connected on a lower electric potential known as cathode. Silver was electrodeposited using a three-electrode electrochemical cell consisting of a platinum counter electrode (anode), an Ag/AgCl reference electrode, and sample as the working electrode (cathode) as shown in the schematic (**Figure 2.6**). The anode and cathode are both connected to an external supply of current. The anode is connected to the positive terminal of the supply, and the cathode (sample to be plated) is connected to the negative terminal. When the current is switched on, the metal cations in the electrolyte move to the cathode, they are reduced by gaining electrons to deposit the article with their metallic, zero valence state.

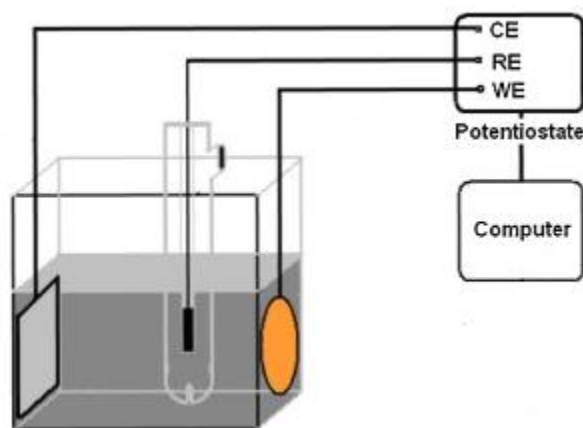


Figure 2.6 – Schematic of the 3-electrode electrodeposition setup

Commercial plating solution of silver (Ag) (Techni Silver CY-LESS II RTU) purchased from Technic, Inc was used as the electrolyte and patterned gold was used as contact to the 3D silver ink scaffold for the working electrode. The sample was immersed in Isopropyl alcohol (IPA) prior to immersion into the aqueous plating solution. IPA lowered the surface tension allowing full penetration of the electrolyte into the complex 3D structure. The electrochemical reaction increased in efficiency when the plating solution was agitated and heated to 40°C during

electrodeposition. At 40°C, we also observed reduction in the grain size of the electrodeposited silver, resulting in smoother surface morphology.

After electroplating, we observed non-conformal silver deposition for constant potential, more deposition in areas of sample closer to the counter electrode due to diffusion limitation. To circumvent the diffusion problem, we employed pulsed electrodeposition technique and optimized it experimentally. The deposition potential was applied for a short interval (-0.55V for 0.5seconds) with off-time for a longer interval (0 V for 3 seconds). The off-time allowed the metal ions in solution to uniformly diffuse throughout the complex 3D scaffold. Using this method, we observed uniform and conformal deposition throughout the structure (**Figure 2.7b**).

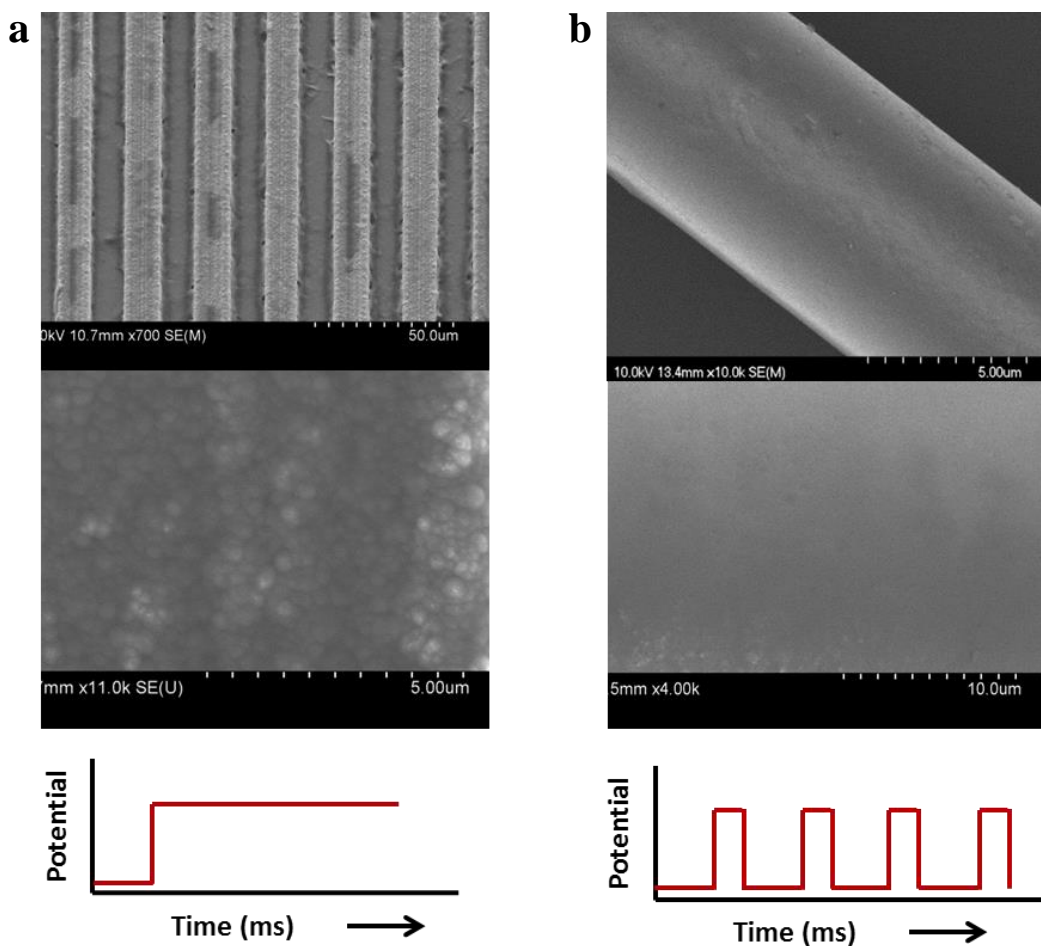


Figure 2.7 – SEM image of silver coating on 1D direct-written line templates when employing (a) a constant potential and (b) a pulsed potential

Figure 2.7 shows SEM images after electrodeposition on silver lines. The dark region shows the area deposited with silver. We can clearly see that the deposition is non-uniform for constant potential. The thickness of the silver film was controlled by the number of iterations of the electrodeposition sequence (one sequence includes one deposition potential and one off-time).

For thick layers of silver, we obtained very smooth coatings (**Figure 2.7b**). However, increase in feature size of the structure results in higher order modes within the structure resulting in modal cutoff in the visible and near-infrared wavelength range⁵⁸. Hence, we want very thin ($\sim 5 \times$ skin depth) and smooth silver layer. Smooth surface is hard to achieve for a thin layer since electrodeposition is conformal and follows the surface morphology of the underlying layer as shown in **Figure 2.8a**. We employed electropolishing to reduce the surface roughness.

2.3.5 *Electropolishing of silver*

By far, the most effective way to electropolish silver is the “peroxide-cyanide bomb”^{59,60}. This process is however highly volatile due to the presence of hydrogen peroxide. The process should only be done in a dedicated glove box designed to handle toxic gases because of the explosive nature of the process and large quantities of hydrogen cyanide that is produced. **(Hydrogen cyanide is very toxic and should always be handled inside a glove box)**. Also, the solution should be made fresh every time to achieve good polishing results.

In this work, we employed a much safer and non-toxic electrolytic solution for anodically producing a smooth silver surface through electropolishing. The principle carrier electrolyte was thiourea, which is then stabilized using larger quantities of a reducing sugar (glucose)^{61,62}. In addition, the electrolyte uses an activating acid (methane sulfonic acid) to activate the thiourea

solution and urea to promote uniform dissolution of elements and provide solution conductivity⁶³. Glycerin is used as a surfactant to reduce the surface tension between the sample and the electrolyte to facilitate uniform electropolishing. The electropolishing solution is environmentally safe, operates over a broad range of current density, fast, and most importantly is functional on irregular shapes and complex designs.

The electrolyte consists of

- a. thiourea: 100 grams per liter of solution;
- b. glucose: 100 grams per liter of solution;
- c. urea: 50 grams per liter of solution;
- d. methane sulfonic acid: 20 milliliter per liter of solution; and
- e. glycerin: 50 milliliter per liter of solution.

First, a volume of millipore water is placed in a vessel equal to one-half of the desired final solution volume. The water is warmed to a temp of $\sim 38^{\circ}\text{C}$ on a hot plate with mechanical stirring. Thiourea and glucose is then added to the water slowly which cools the solution. It is desirable to maintain the temperature of $\sim 38^{\circ}\text{C}$ while adding the thiourea and glucose for better results. The solution temperature falls to $\sim 30^{\circ}\text{C}$ after thiourea and reducing sugar have all dissolved. Methane sulfonic acid is added slowly followed by glycerin. The sample is made anode (working electrode) with platinum as counter electrode as shown in **Figure 2.6**. We do not use a reference electrode here.

The electrolyte temperature is maintained at $\sim 30^{\circ}\text{C}$ with constant mechanical agitation of 450 rotations per min throughout the polishing. We employed a pulsed potential in the range 5V-8V to facilitate uniform electropolishing. SEM was used to characterize the quality of the electropolishing. Best results were obtained when the deposition potential was applied for a very

short interval (7V for 40.0 ms) and off-time for a larger interval (0 V for 16.0 seconds) with black finish observed for high current or slow agitation (**Figure 2.8b**).

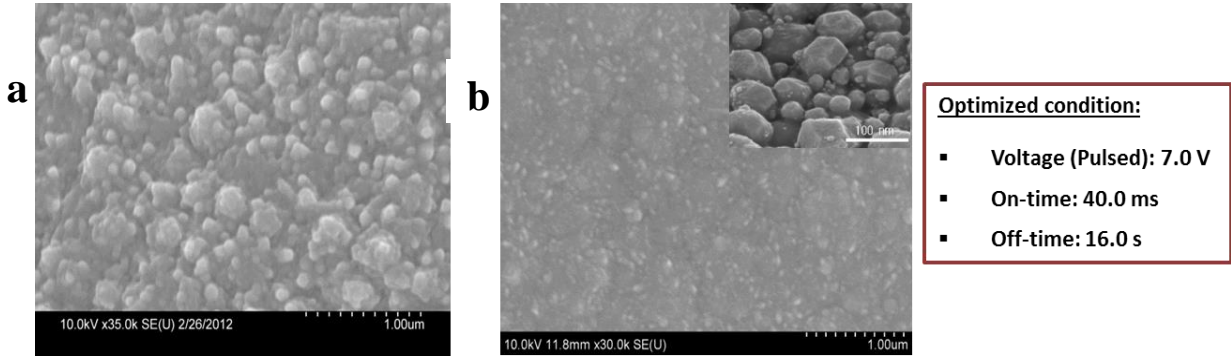


Figure 2.8 – Top view SEM images of silver coating after (a) electroplating of very thin silver layer (~130 nm) (b) electropolishing. Inset shows the magnified view.

After electropolishing, the surface is still not quite as smooth as we want (**Figure 2.8b Inset**). Hence, we further optimized the surface roughness and overall quality of the silver coating via thermal annealing.

2.3.6 Thermal annealing and its effect on the silver coating

Post-thermal annealing is a popular technique used in plasmonics to improve metal's optical and electrical quality⁶⁴. The quality of the silver coating was significantly improved by thermal annealing at 200°C in forming gas (5%H₂ in Ar) for 20 mins (ramp rate 2°C/min). **Figure 2.9a** shows a significant increase in the reflectance spectra of the annealed silver films in comparison to as deposited (electroplated + electropolished). After thermal annealing, the dimensions of the silver increase significantly, suggesting sintering and coarsening processes are active. This welding of the particles and disappearance of the voids and discontinuities (**Figure 2.9c**) responsible for scattering, results in an overall film quality improvement. The average electrical resistivity of the annealed silver films measured by four-point probe is $4.83 \times 10^{-6} \Omega \cdot$

cm. This value is an order of magnitude lower than before annealing ($1.57 \times 10^{-5} \Omega \cdot \text{cm}$) and approaches near bulk silver resistivity ($\sim 1.59 \times 10^{-6} \Omega \cdot \text{cm}$).

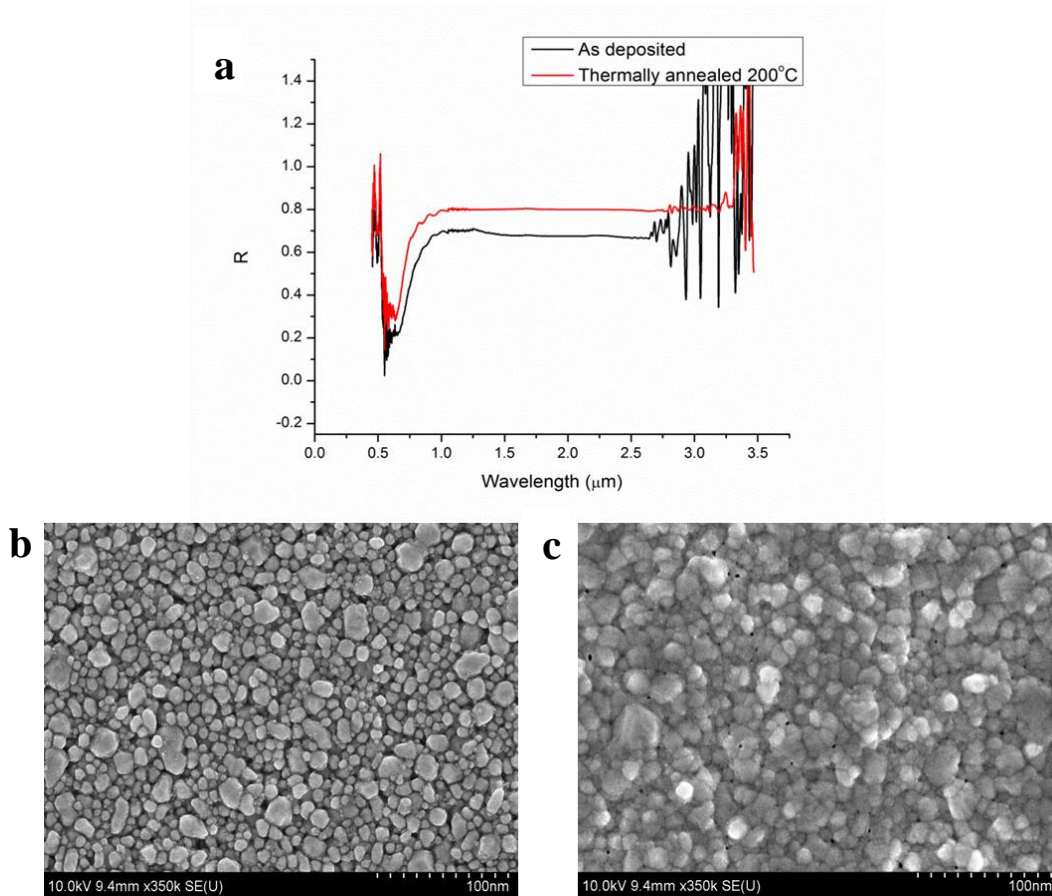


Figure 2.9 – (a) Reflectance spectra of a flat silver coating after annealing. Top view SEM images of silver coating after (b) electroplating + electropolishing and (c) thermal annealing.

Atomic-force microscopy was used to quantify the surface morphology evolution of the deposited silver films during the optimization. All AFM images were obtained with an Asylum Research MFP-3D system. The samples were scanned using tapping mode, typically over a $5 \times 5 \mu\text{m}^2$ area at a scan rate of 1 Hz. AFM scans show a significant decrease in the surface roughness of the silver films (**Figure 2.10**).

After optimizing the silver coating, we deposit a very thin layer of amorphous silicon on the 3D silver template via CVD.

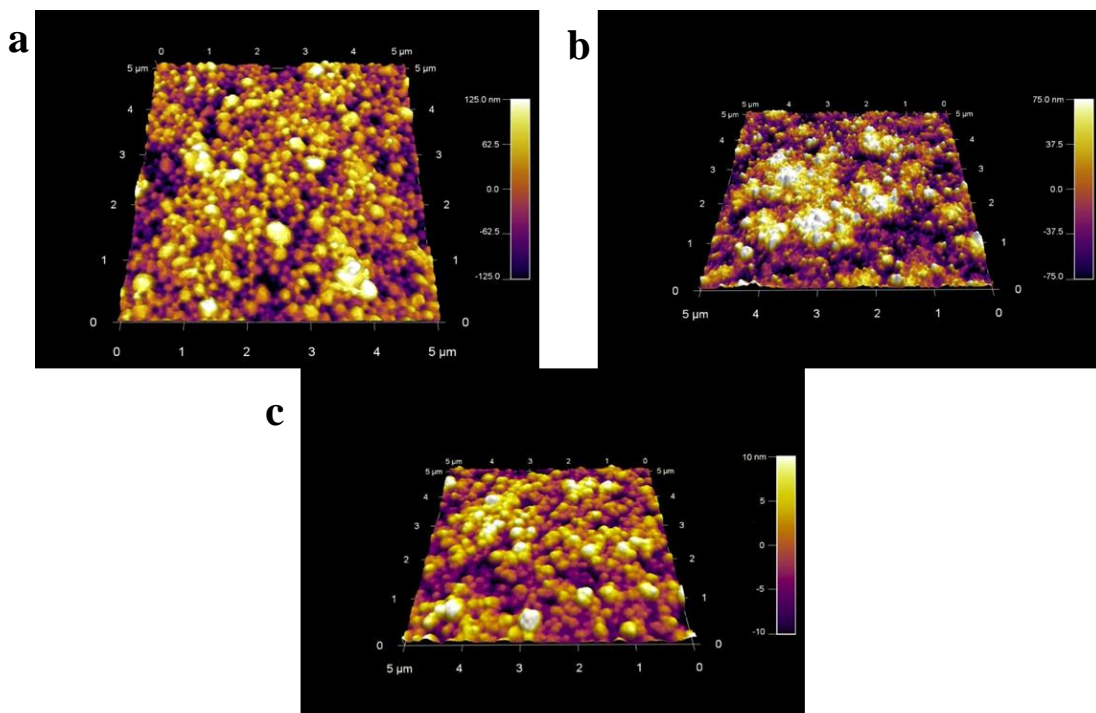


Figure 2.10 – AFM profile showing the reduced roughness of flat silver films after (a) direct-ink writing. (b) electroplating + electropolishing and (c) thermal annealing. RMS roughness: (a) ~70 nm, (b) ~15 nm and (c) ~5 nm

2.3.7 Chemical Vapor Deposition (CVD) of silicon

A thin conformal film of high-quality, low-roughness amorphous Si was deposited around the 3D template using a static chemical vapor deposition (CVD) system^{65,90} with disilane (Si_2H_6 , 98%, Gelest) as a silicon source at 350°C (~50 mbarr, heating rate 8°C min⁻¹) inside a furnace. A static CVD system, where the reacting gas was confined in a cell together with the sample, was utilized since low pressure CVD systems show negligible growth rates at this temperature⁶⁶. The decomposition time controlled the thickness of the silicon film. A 5 hr run at 350°C deposited $\sim 70 \pm 5$ nm of a-silicon which was later confirmed using SEM. It was also observed that higher pressures did not significantly increase the growth rate, while samples prepared at higher pressures had a tendency to peel off the substrate. Because of the static CVD

setup, it was necessary to grow the silicon in several cycles rather than one longer run, because the reaction products are not removed from the chamber and eventually the reaction reaches equilibrium. For silicon thickness of $\sim 200\text{nm}$, three cycles were performed and was later confirmed using SEM.

2.3.8 *Electroless plating of silver*

The amorphous silicon is nonconductive. There are various methods to coat silver on a nonconductive substrate such as sputtering, plating, chemical vapor deposition, etc. All of these techniques have their own pros and cons. The most commonly used method in plasmonics is plating, due to its ease of operation, capability to coat thick and isotropic coating, and low cost. In this work, we employ electroless plating to achieve conformal coating of the third metal layer onto the complex 3D woodpile structure. This technique has several disadvantages. The first is the structure is not completely metallic, but a coated structure only. For our purposes, this should not be a problem as long as the thickness of the coating is larger than the skin depth of the incident light. The second major problem is that electroless plating is not selective. That means that the electroless technique would plate both the structure and the substrate at the same time. To perform transmission measurements for characterization purposes, it is important to selectively coat the structure and not the entire substrate.

Selectivity is a major problem for electroless plating. Many techniques have been developed to overcome this problem, mostly by modifying the substrate surface properties to achieve selectivity. However, these techniques⁶⁷ require complicated chemical modification steps as well as long treatment times. Radke et al's overcame this problem using a rod to transfer the silver coated structure from one substrate to a clean substrate⁶⁸. The transfer part is the most

challenging as structures can easily break and degrade in quality when not handled properly. In this work, we employed a novel and simple approach using radio frequency plasma pretreatment of the sample prior to plating to achieve selectivity⁶⁹.

Electroless plating is the deposition of metals on a catalytic surface which takes place in an aqueous solution without any external source of current. The metal is reduced from its ionic form by a reducing agent which is added into the solution, before it is deposited on the sample surface. The quality of the film is mainly determined by the adhesion between the surface and metal nanoparticles. In this work, we employ the most widely used electroless technique based on Tollens reaction⁷⁰. Here we explain the plating procedure in detail.

1) *Prepare water bath:* Water bath is heated to a temperature of 50°C using a hot plate. This speeds up the plating process.

2) *Prepare chemicals:*

- a) Silver nitrate solution (AgNO_3): The 0.1mol/L silver nitrate solution is 1:1 diluted with millipore water to get concentration 0.05mol/L.
- b) Aqueous ammonia (NH_4OH)
- c) Reducer solution: Glucose ($\text{C}_6\text{H}_{12}\text{O}_6$)

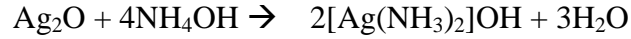
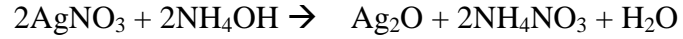
3) *Sample preparation: Surface treatment for adhesion improvement*

- The sample is immersed in an acidic solution of Tin (II) chloride (SnCl_2):
 $\text{SnCl}_2 : \text{HCl} : \text{CH}_3\text{COOH}$ (2 : 1: 3) diluted 1:1 in distilled water.
- Immersed for ~ 10 mins and thoroughly rinsed in distilled running water.
- Treat the sample with RF plasma: dose of 800J

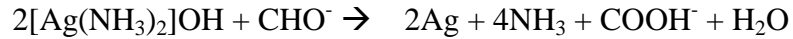
4) *Plating*

- Add the diluted silver nitrate solution to a beaker.
- Add ammonia solution drop by drop with magnetic stirrer set at 150 rpm. As ammonia was added, silver oxide (Ag_2O) precipitate was first produced and then disappeared as more ammonia was introduced to the solution. Once the precipitate

disappeared completely, stop adding ammonia. This is due to the formation of Ammonical silver nitrate complex as shown below



- Place the surface treated sample onto the beaker with the stirrer and add 1 ml of glucose solution. Glucose acts as the reducing agent to give pure silver as can be observed as the sample gets coated



- Remove the sample every 5 mins to rinse it thoroughly with high pressure DI water and repeat the step before the solution gets too muddy.

As mentioned earlier, surface roughness is critical to plasmonic structures and can affect the optical quality of the structures. However, the surface roughness of the third metal layer is not as critical for our application as it is the metal/dielectric interface where surface plasmons exist and propagate. The quality of the adhesion between the surface and the metal coating is what we care the most. Hence, the plating parameters were optimized experimentally based on the quality of the metal/dielectric interface. **Figure 2.11** shows a very good adhesion.

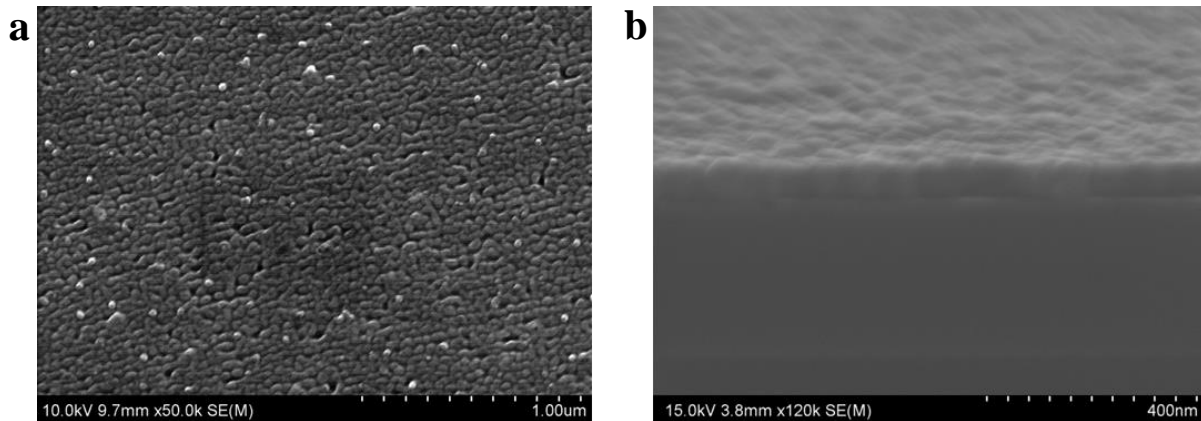


Figure 2.11 – SEM image of silver coating on amorphous silicon via electroless plating (a) top view and (b) cross-section view. Image on the right also shows the high uniformity of the deposition.

Our goal is to use electroless plating on a complex 3D RGWN structure. To demonstrate the 3D coating capability, we fabricated silicon inverse opal structure and coated the structure with silver via electroless plating (**Figure 2.12**). We can see that silver is coated conformally and uniformly throughout the structure.

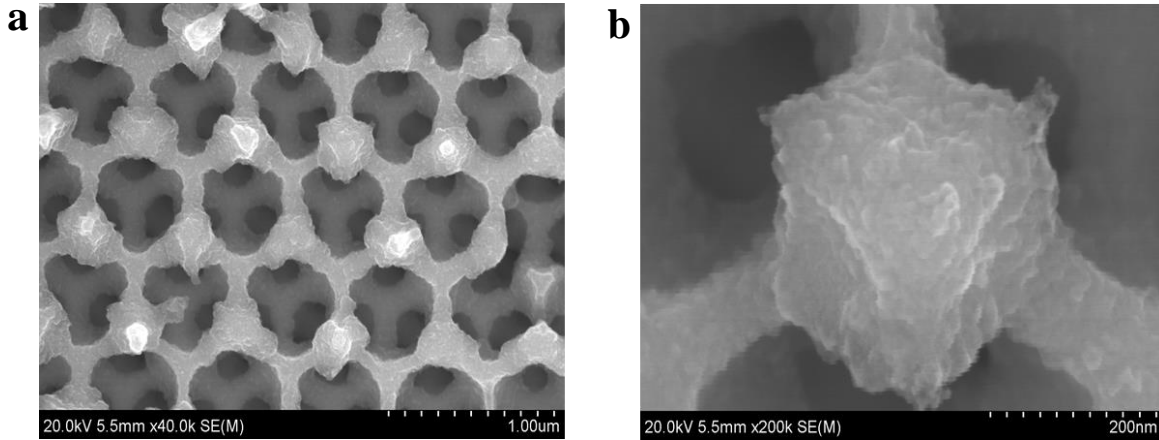


Figure 2.12 – SEM image of silver coating on silicon inverse opals via electroless plating (a) top view and (b) magnified view.

2.4 Final structure

After optimizing all the experimental steps, we fabricated the 3D RGWN structure based on a 3D woodpile scaffold. In addition, various factors were considered while fabricating the structure such as the propagation length of surface plasmons in our MIM structure, the characterization scheme, the beam spot size used for characterization...etc.

The schematic of the final structure is shown below (**Figure 2.13**). The structure consists of a 6-layer 3D woodpile with overall lateral dimension of $250\text{ }\mu\text{m} \times 250\text{ }\mu\text{m}$. The rods are $2.5\text{ }\mu\text{m}$ in diameter with a center-to-center rod spacing d of $\sim 5.5\text{ }\mu\text{m}$.

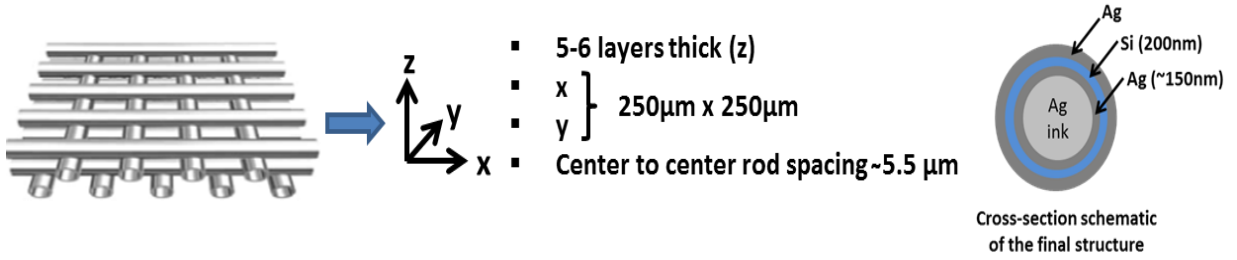


Figure 2.13 – Schematic of the final 3D RGWN structure.

As explained later in Section 3.4, we plan to analyze the transmission measurements to study the optical dispersion within the 3D RGWN structure. In other words, we only want to detect the signal that goes through the structure. Hence, we infill the structure with silver via electroplating as the final structure is a mesh-like structure (**Figure 2.14b**). This eliminates any background signal which can arise from multiple scattering within the woodpile structure.

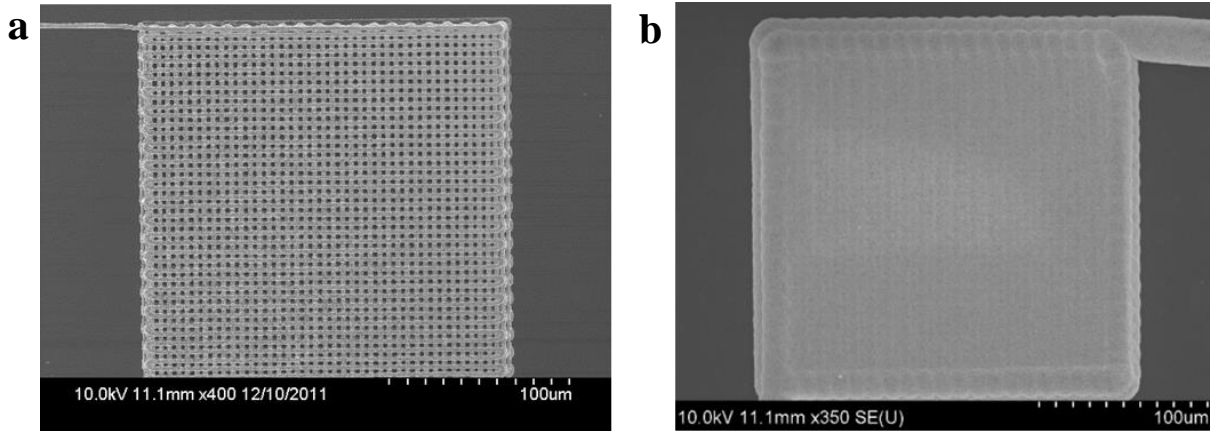


Figure 2.14 – SEM image of the final 3D-woodpile RGWN structure (a) top view and (b) top view after complete infilling of the structure with silver via electrodeposition.

CHAPTER 3

OPTICAL CHARACTERIZATION OF 3D RGWNs

3.1 Introduction

Optical spectroscopy is one of the most common techniques to characterize dispersive photonic materials. Transmittance and reflectance measurements can reveal how light propagates and is manipulated through the structure. Within the set of techniques available for optical spectroscopy, angle resolved spectroscopy is the most common and straightforward technique to study the optical dispersion within photonic materials. It has been used in the past to map out the dispersion relations of 2D⁷¹ and 3D⁷² photonic crystals. This technique is ideal to characterize RGWNs that exhibit wave dispersion and photonic band gaps due to interference effects within the local network.

In this chapter, we introduce realization and in-depth description of the main experimental technique used to characterize 3D RGWNs. Such technique is based on direct inspection of the spatial optical Fourier transform of the response of the dispersive medium (the sample). In short, we will use angular resolved transmission data to study the optical dispersion within these structures by mapping out its photonic band diagram. We also present some preliminary finite difference time domain (FDTD) simulation results to validate the feasibility of our experimental technique based on the theoretical structure constructed from optical measurements and scanning electron microscopy (SEM).

3.2 Optical response of the silver coating (optimized)

As discussed in Section 1.3.3, we fabricated a 1D silver line grating to study the plasmonic response of our final silver coating since SPPs do not directly couple to an optical field. We first printed 1D line gratings with the silver ink using direct writing onto two samples. One of the samples was then electroplated with silver, electropolished and annealed for optimization as discussed in Section 2.3. The grating (**Figure 3.1a**) was coated with ~130 nm of silver coating which was later confirmed by cross-sectional SEM image.

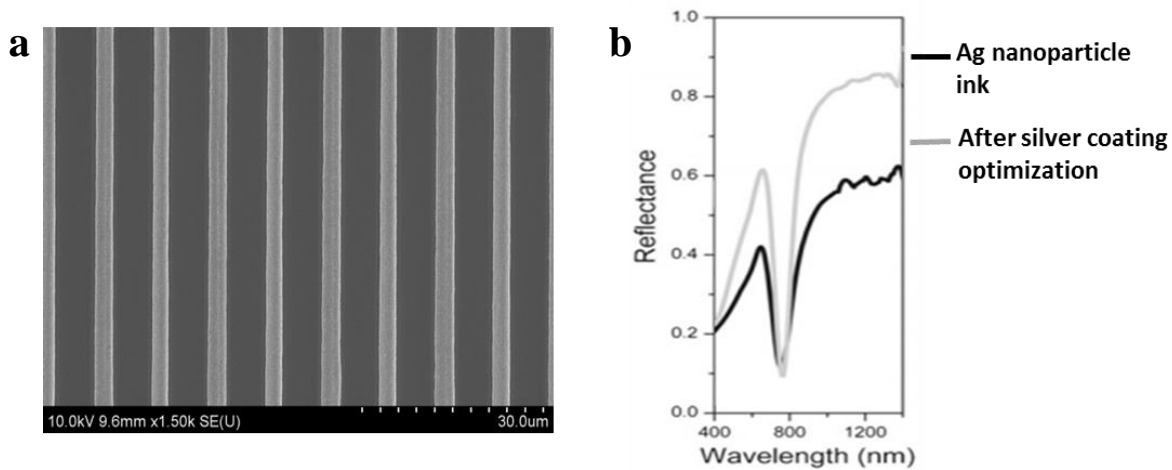


Figure 3.1 – (a) Top view SEM image of 1D line grating coated with silver (optimized). (b) Reflectance spectra of the plasmonic grating after silver coating compared to as printed Ag nanoparticle ink.

Figure 3.1b shows a significant increase in reflectance and a much narrow and sharper resonance peak after silver coating compared to the as printed silver ink. This enhancement in the plasmon response of the grating is an indication of the improved optical quality of the structure after silver coating in comparison to the as printed structure. The resonance peak shifts very little to the right which is expected due to an increase in the feature size of the grating after the coating.

3.3 Experimental realization

As mentioned earlier in Section 2.2, the photonic band structure of RGWNs is only due to dispersion resulting from the network topology. Hence, we want to verify that we get different dispersion by varying the local network topology such as the waveguide length (L) or the sub-wavelength MIM gap (d). FDTD simulations verify that we should get different dispersion with different network topology for such structures as shown in **Figure 3.2**.

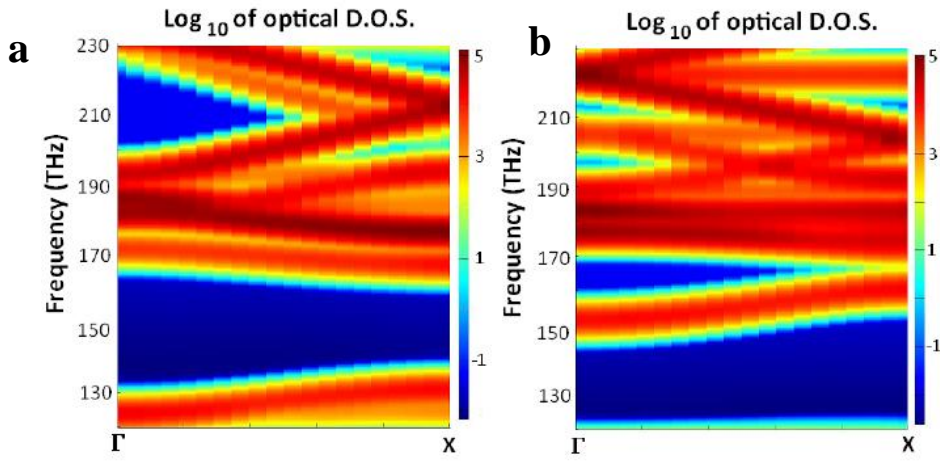


Figure 3.2 – Optical DOS of an infinite 3D network spaced periodically with cubic periodic unit cell (a) $L = 2 \mu\text{m}$ and (b) $L = 2.2 \mu\text{m}$. Image reproduced from Reference 44.

Figure 3.2 plots the optical density of states (DOS) for different wave vectors over frequencies in the near infrared range, where the material dispersion is small. We observe a photonic band structure which is only due to dispersion resulting from the network topology. The k -vectors are extracted from the frequency spectrum at different incident angle.

3.3.1 FIB to open the structure

After fabrication, the 3D RGWN is a closed structure. We open the structure to couple light into the MIM waveguide structure to study the wave dynamics within the structure. We

achieve this using Focused ion beam (FIB). The Focused Ion Beam (FIB) system uses a Ga^+ ion beam to raster over the surface of a sample in a similar way as the electron beam in a scanning electron microscope (SEM). The ion beam allows the milling of the sample at well localized sites. This technique is most widely used in the semiconductor industry, materials science to prepare TEM samples, view cross-sectional images of a structure or make modifications to the structures.

The initial idea was to open to structure using FIB cut at different angles (**Figure 3.3a**). We then characterize the samples using Fourier transform infrared spectroscopy (FTIR) at different FIB cut angles. Amorphous silicon is interconnected throughout the structure and the silicon substrate is transparent in IR. Hence, we should expect light output as we couple light into the structure as shown in **Figure 3.3b**. This should allow access to off-normal incidence k-vectors to map out the dispersion (band) diagram over a broad range of k-vectors. However, the sample is tilted during the FIB cut and the high aspect ratio of the cut is very challenging especially for angled cuts. Moreover, if the cuts are not well defined then we cannot access the k-vectors of the structure.

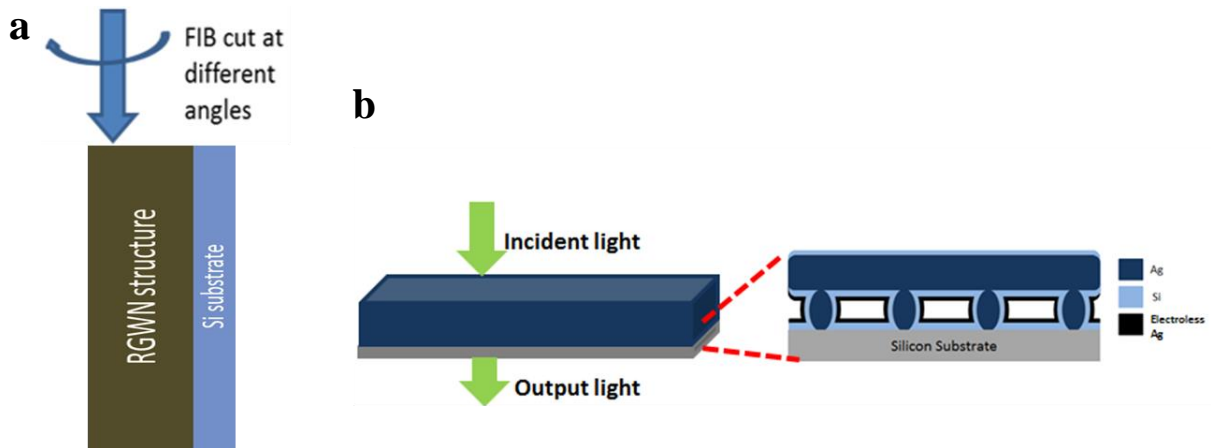


Figure 3.3 – Schematic showing (a) FIB cut at different angles to open the structure. (b) the interconnected silicon throughout the structure.

3.3.2 Angle-resolved Fourier Spectroscopy

The usual and simplest technique for angle resolved spectroscopy consists of the standard normal incidence FTIR setup with two additional branches mounted on a goniometer which are able to rotate in a controlled way around a sample⁷³. An example of this kind of system is shown in **Figure 3.4a**. However, this was a custom built setup and is very challenging to assemble and calibrate. Moreover, we only need transmittance from our structure.

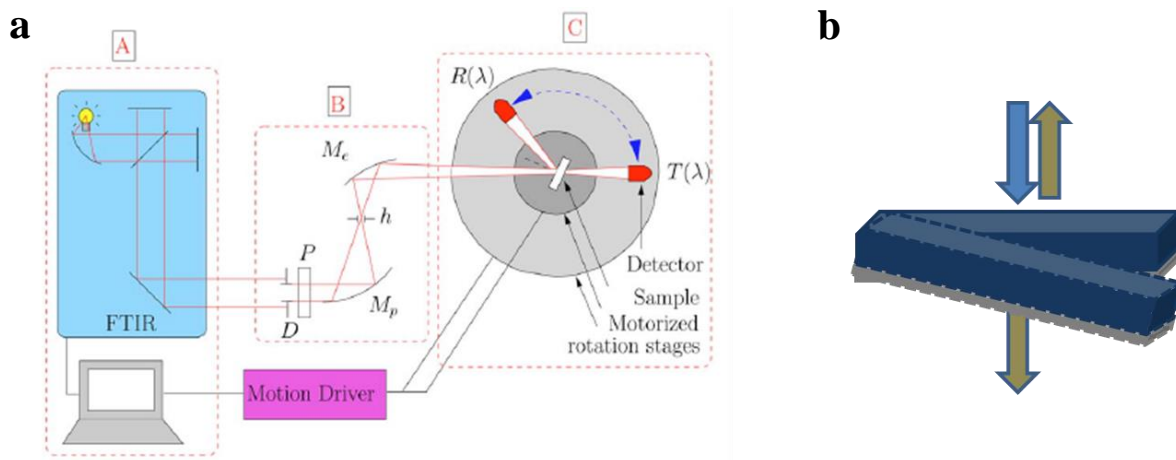


Figure 3.4 – Schematic drawing of (a) the setup for angle-resolved transmission and reflection optical measurements: A, FTIR spectrometer; B, achromatic optical focusing system; C, sample and detector rotation stages. Image reproduced from Reference 73. (b) angle-resolved spectroscopy with only the sample rotated at defined angles to access the off-normal incidence k-vectors.

Instead of doing the angled cuts via FIB or use a complicated setup as shown above, a flat (0°) cut was made and the sample was rotated at defined angles to access the off-normal incidence k-vectors (**Figure 3.4b**). Note that this setup cannot be used for angle-resolved reflection measurements. The idea here is to use a pinhole setup that provides a narrow beam configuration for the measurement of photonic band gaps (PBGs) and this technique has been used in the past to plot photonic band structure of a complex 3D structure⁷⁴. The drawback of this technique is that as the plane waves hit different waveguide at different times, we lose

coherence (phase information) when light excites the sample at different angle. This is true for free space but the coherence is maintained at the point of incoupling for the coaxial configuration as shown in **Figure 3.5**. The red lines are the monitors where the data was collected and analyzed. The plots show the real part of the longitudinal component of the H-field.

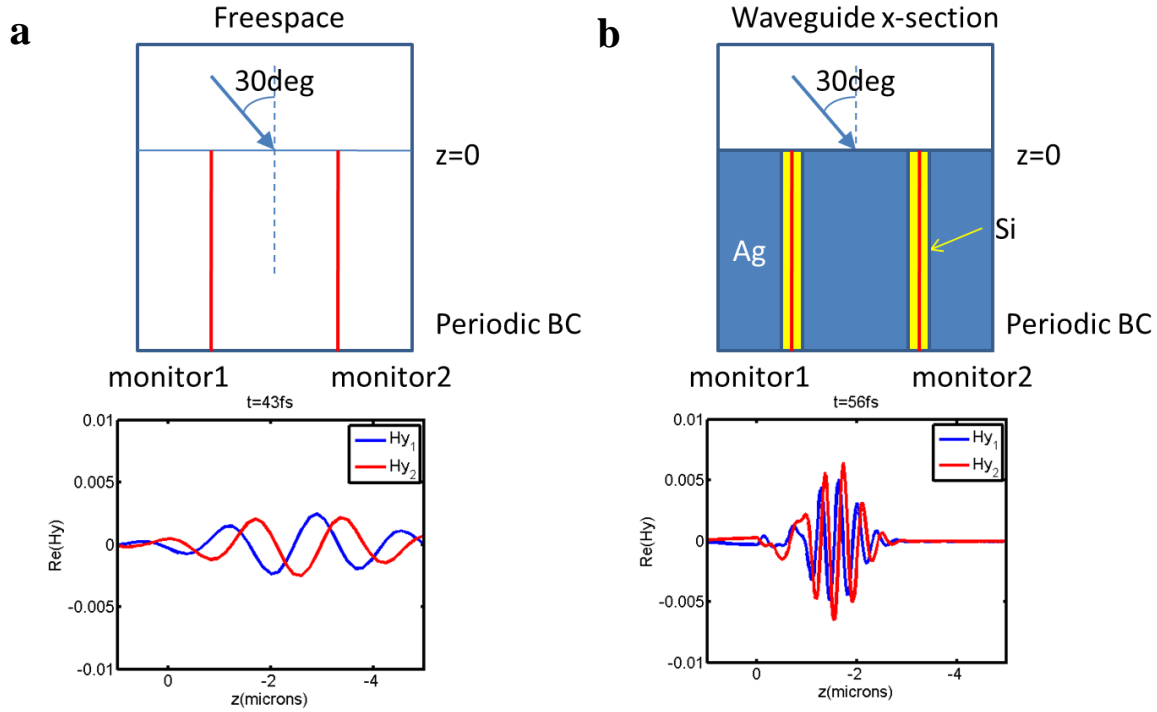


Figure 3.5 – Top: Schematic diagram showing the FDTD simulation setup used to analyze the coherence simulation for (a) freespace and (b) the coaxial MIM geometry. **Bottom:** Real part of the longitudinal H-field as a function of the distance light travels within a material (z) for (a) freespace and (b) for the coaxial MIM geometry.

For freespace, we can see that a $1.5\ \mu\text{m}$ pulse hits monitor2 first and has a phase advance with respect to monitor1, thus defining a k -vector. Note that for a continuous wave (CW) this would be the other way around, but the important thing here is that there is a phase difference. Similar dynamics are observed for a $1.5\ \mu\text{m}$ pulse hitting a waveguide array. Thus, the incoupling does not cause decoherence of the incoming phase, allowing for the structure to have a k -vector.

Minor modifications were made to a Hyperion 2000 IR microscope (Bruker Optics) which was equipped with Cassegrain objectives (15x/0.4) and a liquid nitrogen cooled HgCdTe detector that was available at our lab. The Cassegrain objective of the microscope provides a hollow light cone. First, the numerical aperture (opening angle) of the 15x Cassegrain objective was reduced which acts as the illuminating condenser and sits below the sample. In the standard configuration, the objective illuminates the sample with a hollow cone of wave vectors varying from 10° to 24° (**Figure 3.6a**). Circular disks out of 0.2 mm sheet steel with the same diameter as the top of the Cassegrain objective were cut with a circular hole to serve as an aperture, reducing the opening angle of the illuminating light cone to e.g. 5° or 10° (**Figure 3.6b**).

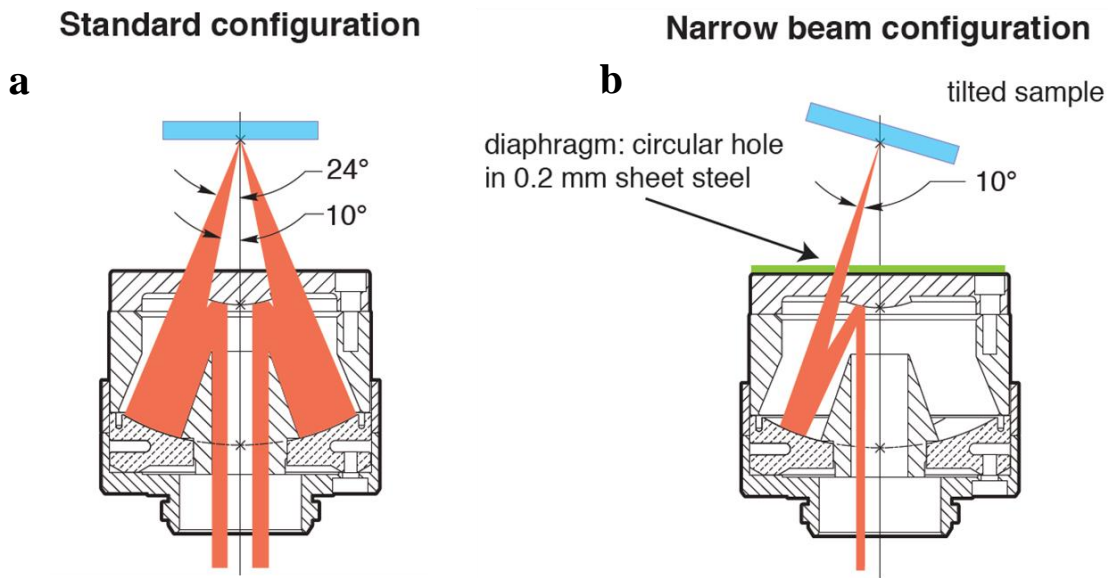


Figure 3.6 – Schematic showing (a) the Standard configuration and (b) the Narrow beam configuration for the Cassegrain objective. Image reproduced from the Newport website.

For proper placement of the holes, we obtained a technical drawing of our objective from the Newport website. During the experiment, one of the sheet steel disks is placed on top of the objective as shown in **Figure 3.7a**. Since the disk had the same diameter as the objective,

centering it was easy. As you can also see from **Figure 3.6**, the narrow beam now hits the sample at an angle. To compensate for that and to vary the angle of incidence in a controlled way, a small goniometer stage from Thorlabs (GN05) and attached a small self-built extension arm to it for mounting the sample (**Figure 3.7b**). The sample wasn't actually located at the virtual fix-point of rotation of the goniometer, so changing the angle of incidence would also move the structure laterally relative to the beam. This made measurements slightly awkward but we couldn't find a way around it in the limited vertical space that was available between the illuminating and collecting Cassegrain objectives.

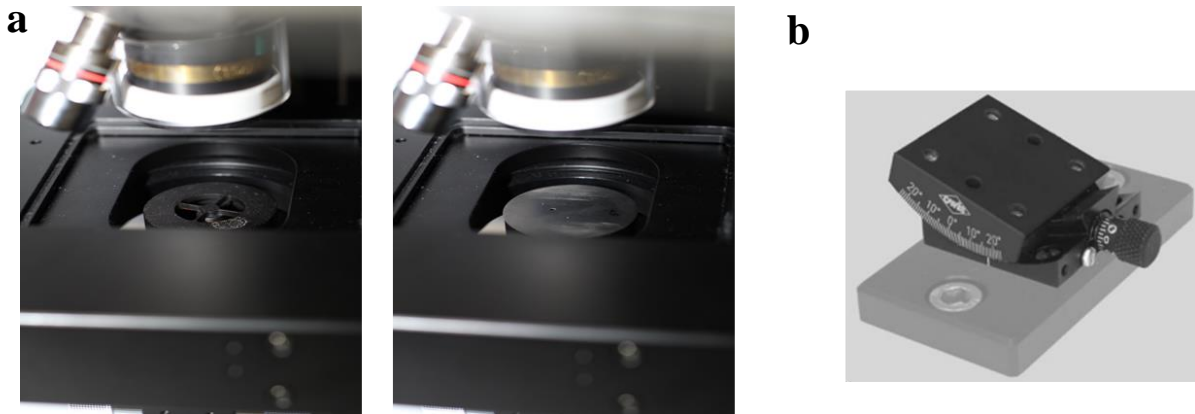


Figure 3.7 – (a) Pinhole setup with 0.2 mm sheet steel with the same diameter as the Cassegrain objective on top of the objective. (b) goniometer stage.

CHAPTER 4

CONCLUSION AND FUTURE OUTLOOK

4.1 Conclusion

The search for new photonic materials has defined important directions for controlling optical dispersion. RGWNs offer a different approach for designing dispersive photonic materials. Resonant guided wave networks are a new class of artificial photonic material, distinct from photonic crystals and metamaterials, in which localized waves resonate in closed paths throughout a network of isolated waveguides connected by power splitting junctions, enabling the wave dispersion to be dependent on the waveguide network layout. The coherent wave propagation through the network is dependent only by the waveguide length and the phase shift upon power splitting and thus opens up new directions for the design of artificial optical materials and devices.

In this thesis, we first introduce the underlying physics of the RGWNs building blocks. The wave dynamics is investigated using a FDTD model. The fabrication of 3D MIM RGWN structures has been developed. FDTD simulation was used to incorporate fabrication limitation to the model while ensuring coherent wave propagation and resonant behavior within these structures. The fabrication process is based on direct writing of a scaffold and subsequent thermal annealing, selective silver plating and CVD to form novel 3D metallic structures. We fabricated the 3D RGWN structure based on optimized experimental procedure. A set of experiments to optimize the plating parameters in order to achieve the smallest surface roughness with high degree of control over the thickness have also been performed. We achieved high

quality films with rms roughness $\sim 5\text{nm}$. A rougher surface leads to more energy loss due to scattering so it is not desirable.

We measured the thickness ($\sim 130\text{nm}$, skin depth $\sim 40\text{nm}$) and resistivity ($4.83 \times 10^{-6} \Omega \cdot \text{cm}$) of the silver coating under optimal conditions. FTIR characterization was performed to obtain the transmittance spectra of silver coated 1D line gratings. The results show good plasmonic response, verifying the high quality of the coating and feasibility of the technique.

We then introduce realization and in-depth description of the main experimental technique used to characterize 3D RGWNs. Angle-dependent Fourier spectroscopy is used to characterize the structure. We also present some preliminary finite difference time domain (FDTD) simulation results to validate the feasibility of our experimental technique based on the theoretical structure constructed from optical measurements and scanning electron microscopy (SEM). Minor modifications were made to a standard Hyperion 2000 IR microscope (Bruker Optics) to incorporate a pinhole setup that provides a narrow beam configuration for the measurement of photonic band gaps (PBGs).

In addition, incorporating more components into the RGWN could allow for more complex devices or alternatively for devices with enhanced performance allowing for the implementation of complex optical functions and could possibly open new opportunities in the design of photonic circuitry devices.

4.2 Future outlook

4.2.1 Fabrication

As discussed in Section 2.3.1, the minimum feature size we can obtain via direct writing is $\sim 2.5 \mu\text{m}$. The ideal feature size we desire is $\sim 1 \mu\text{m}$ for the RGWN structure to suppress any higher order modes. To circumvent this problem, we can use direct laser writing (DLW) to fabricate the 3D woodpile scaffold. DLW is the only technique that allows arbitrary three dimensional micro and nanostructures to be fabricated with sub-100nm resolution⁷⁵ and with a relatively high throughput. The technique utilizes nonlinear optical absorption of a tightly focused pulsed laser beam to selectively crosslink a small volume inside a photosensitive polymer (**Figure 4.1b**). By moving the focal point relative to the sample in all three dimensions, arbitrary three dimensional nanostructures can be fabricated that are not possible through other lithographic technologies. Due to its high resolution, high level of control, low proximity effect, good adhesion and easy handling, TPL has been recently applied to many research areas, such as photonics and plasmonics⁶⁸, biomedical microfluidics⁷⁶ and MEMS devices⁷⁷. A standard optical setup for direct laser writing is shown in **Figure 4.1a**.

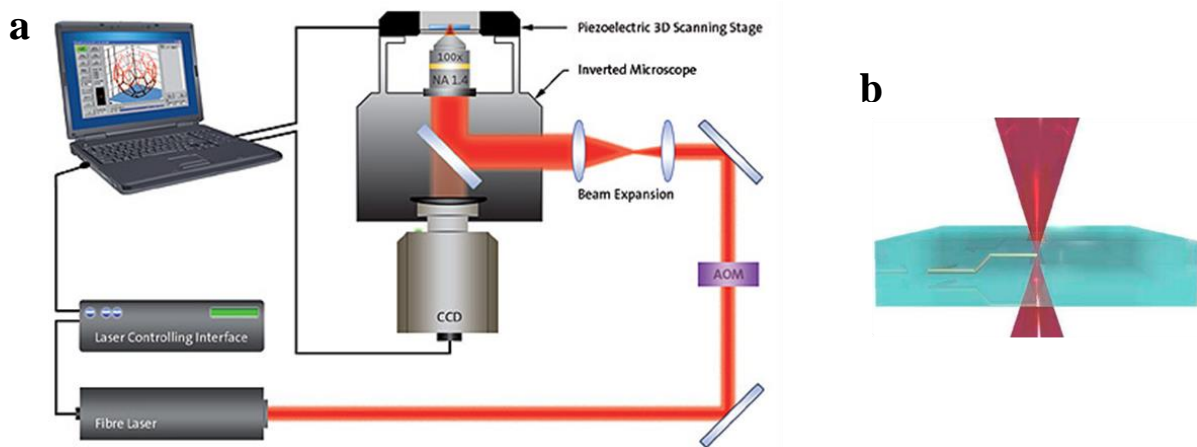


Figure 4.1 – Schematic of (a) a standard Direct-laser writing setup, (b) two-photon polymerization through a photosensitive material.

Once we have a 3D-woodpile polymer scaffold, fabricating the 3D-MIM based RGWN structure is straightforward since we have already optimized all the experimental procedures. Here, we propose three ways to fabricate the structure and the cross-sectional view of the final MIM unit structure is shown in **Figure 4.2**.

Option 1:

- Use electroless technique to coat the 3D scaffold with silver,
- Infill the structure with silver via electroplating,
- Open the structure using FIB, and burn the polymer
- Finally infill the structure with Si via CVD

Option 2:

- Use the polymer structure as a scaffold
- Use electroless technique to coat both the metal layers.

Option 3:

- Use positive tone photoresist to get an inverse polymer woodpile structure
- Use electroless deposition (bottom up) to infill the voids, thus creating the 3D woodpile scaffold,
- Si CVD and electroless Ag deposition.

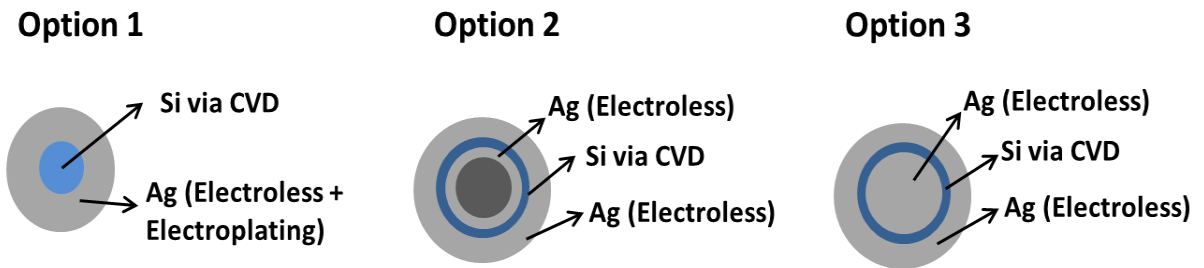


Figure 4.2 – Schematic showing the cross-section view of the different fabrication scheme proposed for the 3D MIM based RGWN structure via direct laser writing. Schematic not to scale.

In addition to the reduced feature size, an advantage of direct laser writing is that the surface morphology of the metal dielectric interface is determined by the surface roughness of the polymer which is atomically smooth. This is very critical for device's performance and eliminates a lot of surface roughness optimization steps.

4.2.2 Characterization

Preliminary characterization on test structures is already underway. As discussed in Section **3.3**, we propose a technique to map out the photonic band diagram of the 3D RGWN structure and study its wave dynamics. FDTD simulation results validate the feasibility of the proposed experimental technique. Using the modified angled-resolved setup, we plan to access the angular frequency of the structure at different off-normal incidence k -vectors to map out its photonic band gap. This is achieved through accessing transmission spectra of the structure at defined angles. We will then compare the experimental results with simulation to verify the novel approach to optical dispersion using these resonant structures.

PART II

PHONON TRANSPORT IN COMPLEX 3D-STRUCTURE (SILICON INVERSE OPALS)*

*This work was done in collaboration with Jun Ma from Sinha Group at MechSE, University of Illinois at Urbana-Champaign.

CHAPTER 5

COHERENT PHONON-GRAIN BOUNDARY SCATTERING IN SILICON INVERSE OPALS*

*Content in this chapter was previously published by the author and reproduced with Permission⁷⁸. Copyright American Chemical Society, 2013.

5.1 Background and general concepts

Thermoelectric materials are promising candidates for high efficiency power generation based on the Seebeck effect or solid-state cooling devices based on the Peltier effect. The performance of a thermoelectric device is governed by the figure of merit $ZT = S^2 \sigma_{\text{eff}} / k_{\text{eff}}$, where S , σ_{eff} , T , and k_{eff} are, respectively, the Seebeck coefficient, effective electrical conductivity, absolute temperature, and the effective thermal conductivity. Thermal transport in these materials is a key factor for device performance since the thermoelectric figure of merit is inversely proportional to thermal conductivity⁷⁹⁻⁸². Nano-structured materials can achieve a much lower thermal conductivity than predicted⁸⁰, mostly through phonon boundary scattering. As a result, nano-structured materials such as single crystal silicon nanowires^{83,84} or membranes of hole arrays^{85,93} exhibit improved thermoelectric performance compared to their bulk counterpart. First, as the size of structure decreases, its surface area to volume ratio increases, thereby increasing the importance of boundaries and interfaces. Additionally, at the nanoscale the characteristic length of the structure approaches the phonon wavelength, and other interesting phenomena such as dispersion relation modification and quantum confinement may arise and further alter the thermal transport. Therefore, understanding thermal transport in nanostructured

materials is crucial for engineering high performance devices. In this thesis, we investigate phonon heat conduction in silicon inverse opal structures.

Sub-micrometer features in periodic dielectric structures^{86,87} give rise to unusual optical properties⁸⁸⁻⁹⁰ and are of great current interest in designing new functionalities in optoelectronics. Phonons, the quanta of lattice vibrations in a dielectric, can similarly interact in interesting ways with periodic nanostructures that possess features below the phonon mean free path and/or comparable to phonon wavelengths. However, phonon transport has major differences from photon transport due to a broadband spectrum and dominant incoherence arising from non-linearity, in addition to the commonly discussed difference in dispersion. Recent investigations of phonon transport in nanostructures focused on the thermal conductivities of two-dimensional “holey” silicon⁹¹⁻⁹³ and core-shell nanowire,⁹⁴⁻⁹⁶ hinting at the possibility of coherent effects in phonon transport. Here we extend the experimental investigation to three-dimensional periodic nanostructures, silicon inverse opals.

The periodicity of inverse opals influences thermal transport in two ways: at continuum or diffusive length scales, heat flow lines bend as they flow through the lattice structure resulting in significant increase in thermal resistance. At microscopic length scales, phonons meandering through the lattice scatter at surfaces and grain boundaries, reducing the intrinsic thermal conductivity of the material. Previous theoretical work on thermal transport in inverse opals⁹⁷ has considered the diffusive regime where the carrier mean free path is much smaller than the feature size. A boundary integral method solution to the continuum heat diffusion equation for inverse opal geometries shows significant deviation from the Maxwell-Garnett formula⁹⁸ for the effective thermal conductivity of a composite. The formula yields the ratio of the effective thermal conductivity to the material thermal conductivity as a function only of porosity and

dimensionality of the structure. The exact solution shows that the geometry of the lattice and the porosity together determine the effective thermal conductivity. We note here that macroscale three-dimensional periodic structures, termed phononic crystals in the literature,^{99,100} attract interest for their acoustic properties and are distinct from the materials investigated here. Our investigation covers features on the order of 10 nm, approximately five orders of magnitude smaller than such acoustic periodic structures and focuses on heat flow instead of acoustics.

In this work, we show that the lattice periodicity of silicon inverse opals mainly influences continuum heat flow and that microscopic effects on phonon conduction occur through scattering at the grain boundary. The scattering of phonons from grain boundaries is commonly assumed to be a frequency-independent process across all temperatures. The assumption leads to a phonon mean free path that is comparable to the grain size. While thermal conductivity data from a wide range of experiments¹⁰¹ support this assumption, recent experimental work shows that this is invalid in the case of nanocrystalline silicon where the scattering rate has an approximately linear dependence in frequency¹⁰². We report measurements on the thermal conductivity of silicon inverse opals with varying feature size that reveal an even stronger dependence of the scattering rate on frequency. We infer that such scattering arises due to coherence in the reflection of phonons from the boundaries of the inter-grain region. A model of thermal conductivity of inverse opals that incorporates both diffusive thermal transport as well as microscopic phonon transport incorporating coherent phonon scattering at grain boundaries, agrees well with the data. We start below with details of fabrication and characterization, and follow with thermal conductivity measurements and transport modeling.

5.2 Fabrication of silicon inverse structures

The fabrication of silicon inverse opals has been discussed by many papers^{90,103}. Here we present an overview of the fabrication procedure (**Figure 5.1**) that was used. We employed the Stober method followed by several regrowth cycles to synthesize silica spheres ranging in diameter from 300-640 nm.¹⁰⁴ Prior to crystal growth, we heat-treated the spheres for 6 h at 600 °C to avoid shrinkage that potentially leads to cracking of the opal structure during post-processing at elevated temperatures.¹⁰⁵ Using a modified vertical deposition method¹⁰⁶ that employs a temperature gradient,¹⁰³ we deposited colloidal crystal films on a single side polished Si substrate (**Figure 5.1A**). After a Piranha clean, substrates were placed at a 20° angle in a 20 mL scintillation vial (Fisher) with 4 g of colloidal dispersion (2-3% w/w in ethanol). The vials were left in an incubator (Fisher, Isotemp 125D) at ~42-45 °C overnight. We noticed that the appropriate temperature window used to grow high quality opals was small and occasionally needed to be experimentally adjusted. Reflection and transmission spectroscopy along with SEM provided measures of the thickness and quality of the samples. We only selected high quality (closely-packed) templates with ~5-8 opal layers for further processing. **Figure 5.2A** shows an SEM of a typical sample.

For such templates, we deposited a thin conformal film of high-quality, low-roughness amorphous Si around the spheres (**Figure 5.1B**) using a static CVD system with disilane (Si_2H_6 , 98%, Gelest) as a silicon source at 350 °C (~50 mbarr, heating rate 8 °C min⁻¹). We controlled the deposition time to make sure that the pores in the opal template were filled to a maximum.¹⁰⁷ Pores in the underlying opal structure are filled to the maximum at 86% once the silicon overlayer starts forming during the fabrication described above.¹⁰⁸ The shell thickness is approximately equal to 6% of the diameter of silica in this case.¹⁰⁹ Scanning electron

microscopy (SEM) provided additional confirmation of this feature size. Samples were annealed in a tube furnace at 1000 °C for 10 hours under forming gas to recrystallize the amorphous silicon. We used reactive ion etching (1 min, 70 W, gasses SF₆ and O₂ 20 sccm, 50 mTorr chamber pressure) to open a 1×2 mm² window defined by a Kapton film (**Figure 5.1C**). This window allows the creation of an interpenetrating network of oxide within the opal template by exposing the silica spheres at the surface when immersed in an ethanolic solution of 5% hydrofluoric acid for ~25-30 mins. Selectively etching only a small region of the sample prevented cracking and sample lift-off. The opal template was completely etched away leaving the silicon inverse opal structure (**Figure 5.1D**). **Figure 5.2B** shows the SEM of a typical sample after RIE and HF etching.

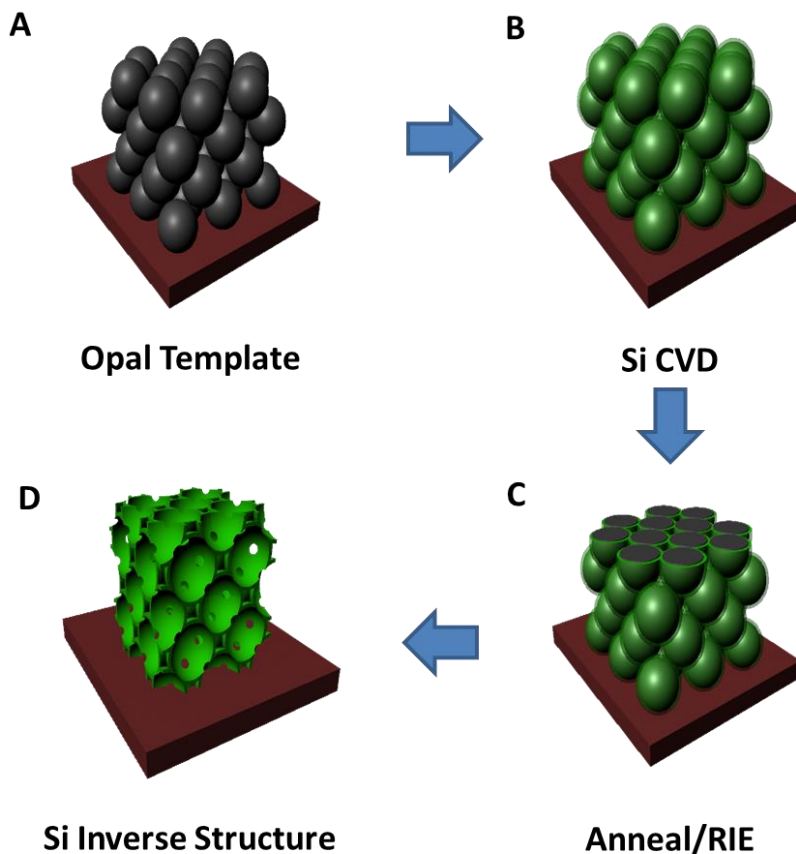


Figure 5.1 – Overview of the silicon inverse opal structure fabrication scheme. **A.** 3D fcc silica opal template. **B.** Silica opal coated with a thin layer of a-Si via CVD. **C.** Annealed sample with RIE to expose silica. **D.** Silicon inverse structure after etching the silica template.

5.3 Shell thickness and grain size characterization

The diameter of silica spheres, D controls two feature sizes in the inverse opal that directly affect phonon heat conduction: The thickness of the silicon shell, d , that controls the phonon mean free path for surface scattering and the nominal size of the grains, l , that controls phonon grain boundary scattering. We have discussed measurement of the shell thickness above and now discuss measurements of the grain size. We anticipate grains to be limited in size by the thickness of the shell.¹¹⁰ Transmission electron microscopy (TEM) confirms polycrystallinity and also reveals atomic scale surface roughness but can only image the grain over a small region.

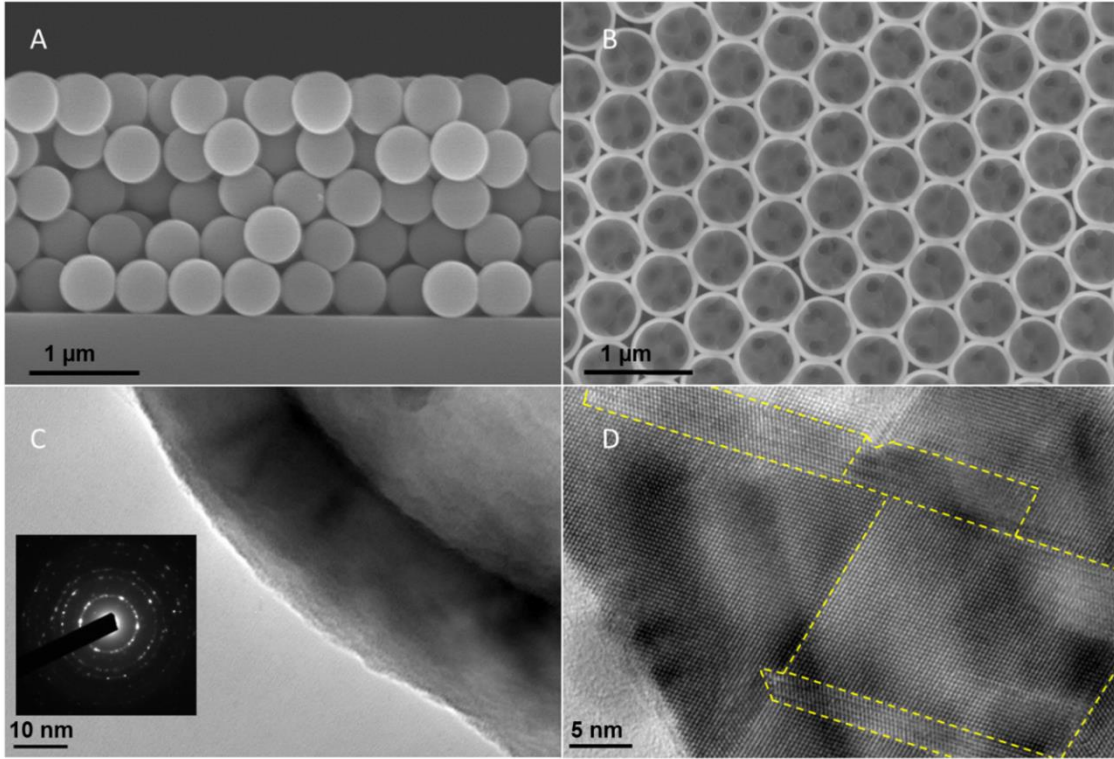


Figure 5.2 – **A.** SEM image of the opal template. **B.** Top view SEM of the structure after RIE opening and HF etching. **C.** TEM showing roughness scale on the surface of the silicon shell. Inset shows selected area diffraction pattern. **D.** High resolution TEM showing the polycrystalline nature of the sample.

Figure 5.2C and **D** show TEMs of a typical sample. We employed X-ray diffraction (XRD) to measure the average grain size across the entire depth of the sample over spot sizes

$\sim 1\text{mm}$ in diameter. A $2\theta-\omega$ scan yields the average crystallite size along the height of the inverse opal layer. The inset of **Figure 5.3** shows the XRD data for a sample fabricated using 420 nm silica spheres. **Figure 5.3** further plots the average grain size for the measured inverse opals as a function of the diameter of the silica spheres used in the fabrication. The systematic trend of the data confirms the hypothesis that grain size is essentially limited by the thickness of the silicon shell. As discussed above, the diameter of the silica spheres directly controls the thickness of the silicon shell. We find the average grain size to decrease from 36 nm (with $D=640$ nm) to 20 nm (with $D=300$ nm). As the diameter of the spheres and consequently the thickness of the silicon shell decreases, the distribution in grain sizes also becomes narrower.

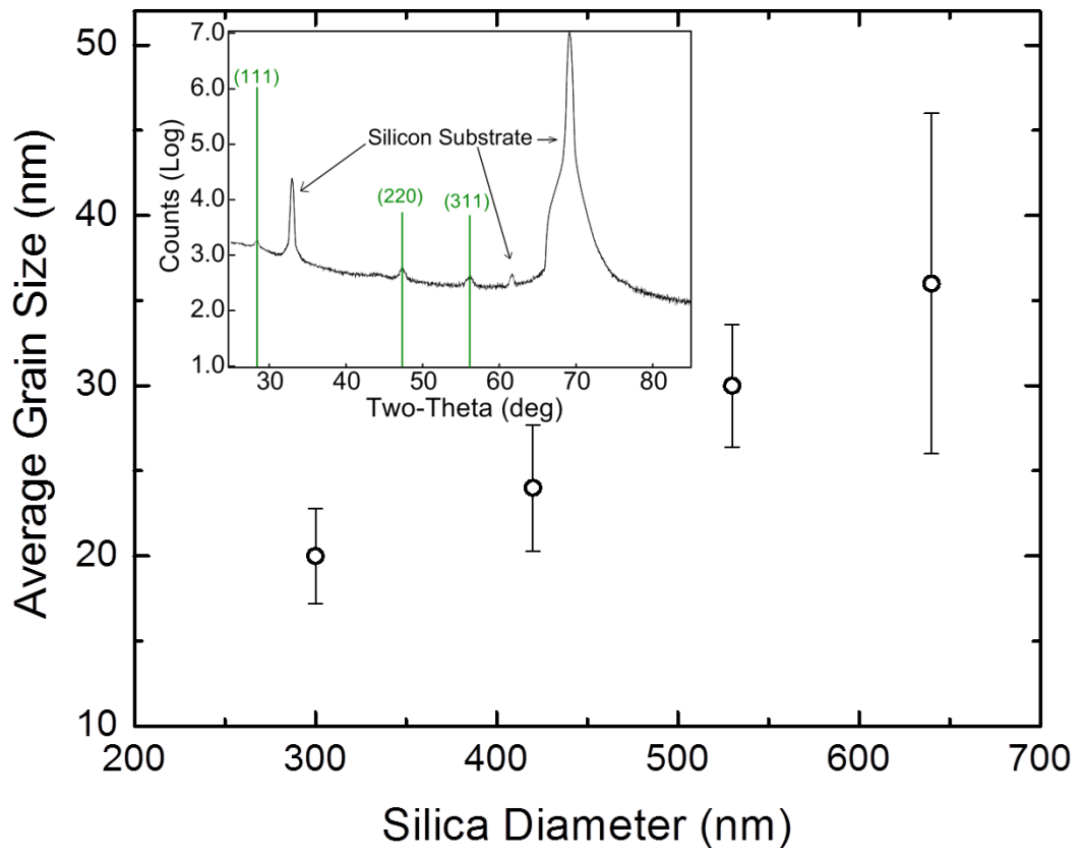


Figure 5.3 – The average grain size from XRD measurements. Inset: XRD profile of a typical silicon inverse opal sample. We average the grain size over three orientations, (111), (220) and (311).

5.4 Thermal conductivity measurements

5.4.1 The 3ω method

Any measurement on thermal conductivity requires two quantities: the heat flow and the temperature gradient. Our samples effectively possess a thin-film geometry with thicknesses in the range 2-6 μm . The frequency domain 3ω method¹¹¹ can readily measure the thermal conductivity of such samples. A 3ω device usually consists of a bulk substrate, a thin film of interest and a heater (thermometer) as shown in **Figure 5.4**. Previous work^{112,113} describes the 3ω method in detail. In brief, a sinusoidal current at a frequency ω through a metallic heater sets up an oscillatory temperature rise, ΔT at the harmonic frequency 2ω . This results in a voltage across the metal line oscillating at frequency 3ω . Measurement of the 3ω voltage via a lock-in amplifier provides ΔT . Comparing the measured ΔT with a model of multilayer heat diffusion¹¹⁴ enables the extraction of thermal conductivity of the sample. We next discuss the design of 3ω measurements for our samples.

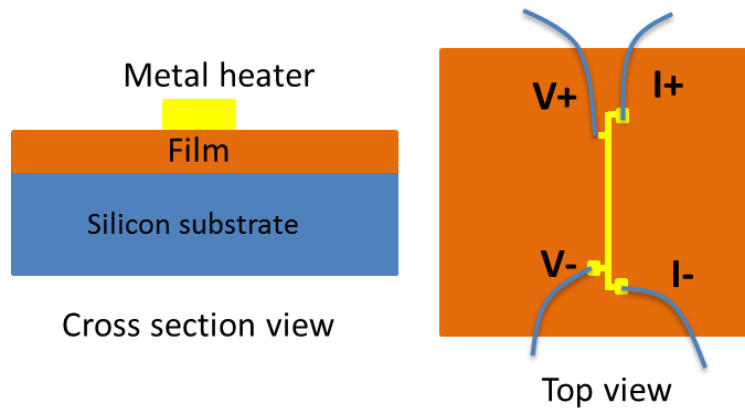


Figure 5.4 – Schematic of a 3ω device.

Based on previous measurements of thin silicon¹¹⁵ and polysilicon films¹¹⁶, we expect the effective room temperature thermal conductivity of the films to be rather small at ~ 1 W/mK on

account of the large porosities. Assuming a thermal conductivity of 1 W/mK and a bulk-like volumetric heat capacity scaled appropriately by the porosity, the expected thermal diffusivity, α is $\sim 3 \times 10^{-2} \text{ cm}^2/\text{s}$ at room temperature. For the typical frequency range of 10-1000 Hz used in 3ω measurements, we estimated the thermal penetration depth to be $\sim 30\text{-}300 \text{ }\mu\text{m}$ at room temperature. This is much larger than the thickness of the inverse opal layer and allows the 3ω measurement to probe the entire thickness of the thin film with the substrate underneath acting as the reference. Heat flow across the sample during the measurement is essentially one-dimensional when the width of the heater is chosen to be greater than the thickness of the sample¹¹². This further simplifies thermal conductivity extraction.

The preparation of samples for the 3ω measurements proceeded as follows. We employed plasma-enhanced chemical vapor deposition (PECVD) to deposit a 100 nm thick silicon dioxide layer on the sample, and patterned a 300 nm thick, 50 μm wide Au heater line through a shadow mask. The heater is thick enough to maintain physical contact with the wavy substrate underneath. The large width compared to the sample thickness ensures one-dimensional heat flow across the sample, as discussed above. Post-measurement cross-sectional SEMs confirmed continuous physical contact across all interfaces.

5.4.2 *Data and discussion*

All layers and interfaces present in the 3ω sample described above contribute to ΔT but the thermal impedance posed by the inverse opal layer dominates over the rest. The thermal diffusivity of the bulk Si substrate is typically more than two orders of magnitude larger than that of the inverse opal layer. At 300 K, we expect the inverse opal layer to dominate and contribute more than 80% of the temperature rise at the heater. Based on previously measured values¹¹⁷, we

estimate impedances from interfaces and the oxide to be small. At 300 K, for example, these contribute <3% to the total temperature rise. Calibration for the measurement involves measurement of the electrical resistance of the heater line at low currents (~250 nA). We use the Bloch-Grüneisen formula¹¹⁸ to fit the electrical resistance of the heater line in the temperature range of 15-400 K. This serves as the calibration for subsequent electrical resistance based thermometry. Differentiating the fit yields the temperature coefficient of resistance, dR/dT of the heater.

During the measurements, we observed a linear relation between ΔT and the logarithm of heater frequency for all temperatures, confirming an essentially one-dimensional heat flow across the inverse opal films. We checked for errors in the one-dimensional approximation by fitting the temperature rise with a two-dimensional multilayer heat diffusion model but found the discrepancy in extracted thermal conductivities to be <0.5%. We note that during the course of a complete temperature sweep (30-400 K), ΔT was always smaller than 2 K for all samples except for the smallest sample at 30 K. In the latter case, ΔT was ~4 K. Since we assume the base temperature of the sample as the temperature of the cryostat, we expect the error in this assumption to be less than 2 K except as noted above. We could not obtain reliable data below 30 K since the resistivity of Au loses sensitivity to temperature.

Figure 5.5 shows the measured effective thermal conductivities (right axis) of four inverse opal samples¹¹⁹. The thickness of the silicon shell and the average grain size in each sample are indicated. All samples possess a relatively low thermal conductivity (~1 W/mK at room temperature) owing to the large porosity and bending of heat flow lines inside the structure as discussed previously. Using numerical solutions obtained in Ref. ⁹⁷, we convert the effective thermal conductivities to the material thermal conductivities. The latter are shown on the left

axis. The thermal conductivity of previously measured undoped LPCVD polysilicon films with $\sim 1\text{-}4\ \mu\text{m}$ thickness¹⁰¹ ranges between $\sim 15\text{-}55\ \text{W/mK}$ at 300 K for grain sizes in the range $\sim 190\text{-}550\ \text{nm}$. Thermal conductivity modeling of this data set revealed that thermal conductivity scales approximately proportional to the grain size. The material thermal conductivities of silicon inverse opals are lower than those of the previous LPCVD thin-films since the grain size in our samples are nearly an order of magnitude smaller than previous samples. However, in contrast to LPCVD thin films, the material thermal conductivities of inverse opals at 300 K do not scale in direct proportion to the grain size when compared with the previously measured values or between our samples. A direct scaling of thermal conductivity with grain size would yield material thermal conductivities of inverse opals in the range $2.8\text{-}5.1\ \text{W/mK}$ at 300K. The measured values are approximately 50% larger. Thus, a grain size dependent mean free path does not explain the thermal conductivity of inverse opals. We now turn to the low temperature data for more insight.

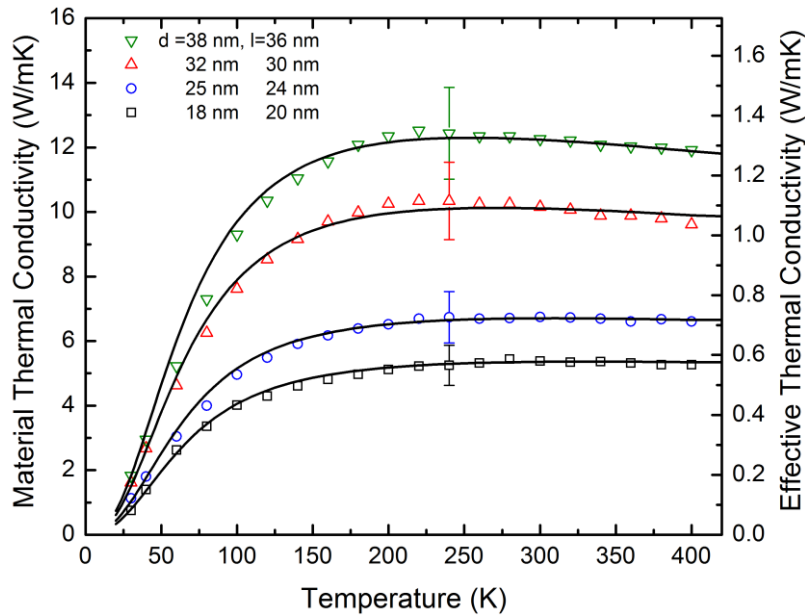


Figure 5.5 – Measured effective (right axis) and material (left axis) thermal conductivities of silicon inverse opals. The fitted curves are calculated from the modified Callaway's model with $\sim \omega^2$ dependence in the phonon grain boundary scattering rate. The error bars on each curve indicate the percentage uncertainty of that sample.

The variation of thermal conductivity with temperature at low temperatures (prior to the strong onset of Umklapp scattering) is indicative of the frequency dependence of the dominant phonon scattering mechanism. Applying results from the kinetic theory, the lattice thermal conductivity of a three-dimensional phonon gas is¹²⁰

$$\kappa = \frac{1}{3} \sum_{j,\omega} C v \Lambda \quad (1)$$

where j represents different phonon modes. The volumetric heat capacity, C , the phonon group velocity, v , and the phonon mean free path, Λ are frequency dependent quantities appearing in the conductivity summation. At low temperatures, if the surface or alternately the grain boundary dominates phonon scattering, the mean free path typically remains independent of the phonon frequency. Thus, the temperature dependence of thermal conductivity follows the well-known $\sim T^3$ dependence of the heat capacity. The thermal conductivity of LPCVD polysilicon films follows such temperature dependence at low temperatures indicating a frequency-independent mean free path arising from grain boundary scattering.

The conductivity data in **Figure 5.5** however, varies as $k \sim T^{1.8}$ at low temperatures. We expect the material in the sample to possess a heat capacity similar to the bulk since lattice dynamics calculations clearly show phonon dispersion and density of states to remain unaltered at these dimensions¹²¹. In silicon inverse opals, surface scattering is equally important as grain boundary scattering since the feature sizes are similar. However, a frequency dependence arising from surface scattering is unlikely since TEM images show atomic scale roughness at the surfaces. In this case, surface scattering should be consistent with the Casimir model^{122,123} and independent of frequency. Thus, the weaker than $\sim T^3$ temperature trend of the data is puzzling at first glance. Using detailed phonon scattering theory below, we show that this trend plausibly

originates from coherence of the reflected phonon in the inter-grain region. This yields a frequency dependence in the grain boundary scattering rate that results in a weaker than $\sim T^3$ dependence in the thermal conductivity data.

5.4.3 Phonon-grain boundary scattering theory

In equating the phonon mean free path with the grain size, there is an implicit assumption that phonons are randomly scattered at all grain boundaries. This is not strictly valid at low temperatures. Phonons scatter near a grain boundary due to change in orientation of crystal planes as well as disorder in the inter-grain region. In a perturbative approach, both induce a perturbation in the wave velocity, Δv . The change in wave velocity leads to back-scattering from mode \mathbf{q} to \mathbf{q}' whose rate is

$$\frac{1}{\tau_g(\mathbf{q})} = \frac{V}{(2\pi)^3} \rho^{-2} \omega^{-2} \sum_{j'} \oint v_g^{-1} 2 |M(\mathbf{q}, \mathbf{q}')|^2 dS' \quad (2)$$

where V is the volume of a crystal containing one boundary, ρ is the density, v_g is the phonon velocity, dS is the surface element, j is polarization. The perturbation element $M(\mathbf{q}, \mathbf{q}')$ is

$$M(\mathbf{q}, \mathbf{q}') = V^{-1} 2 \rho \omega^2 \int d\mathbf{r} \delta v(\mathbf{r}) e^{i\mathbf{Q} \cdot \mathbf{r}} (\boldsymbol{\varepsilon} \cdot \boldsymbol{\varepsilon}') \quad (3)$$

where $\boldsymbol{\varepsilon}$, $\boldsymbol{\varepsilon}'$ are unit vectors along the polarization directions, and $\mathbf{Q} = \mathbf{q}' - \mathbf{q}$. Klemens¹²⁴ showed that randomized scattering at a tilt boundary gives rise to a frequency independent scattering rate

$$\frac{1}{\tau_g} = \frac{2}{3} (v/l) (\Delta v/v)^2 \quad (4)$$

where l is average grain size, Δv is the change in velocity at the tilt boundary. The magnitude of the rate is typically small since $\Delta v/v \sim o(0.1)$. Similar randomized scattering in the inter-grain region with greater disorder leads to much stronger scattering since $\Delta v/v \sim 1$ in this case. However, for scattering to be incoherent, the two boundaries of the inter-grain region should be far apart compared to the phonon wavelength. This suggests a critical frequency, $\omega_{cr} \cong v/t$, below which scattering is increasingly coherent. Here, t is the thickness of the inter-grain region.

For frequencies lower than this critical frequency, the two boundaries scatter phonons coherently. This is especially likely at low temperatures since t is typically $\sim \text{\AA}$ scale and much smaller than phonon wavelengths. The scattering rate in this case has a quadratic frequency dependence¹²⁴,

$$\frac{1}{\tau_g} = \frac{4}{3} \frac{\omega^2 t^2}{v l} (\Delta v / v)^2 \quad (5)$$

where Δv is now the change in velocity due to inter-grain region. We show below that such frequency dependence explains the weaker than $\sim T^3$ dependence in the thermal conductivity of inverse opals.

We also point out recent work on nanocrystalline Si¹⁰² that suggests linear frequency dependence in the grain boundary scattering rate. The expression for the scattering rate in this case is proportional to the phonon transmission coefficient of the grain boundary. Atomistic simulations¹²⁵ reveal that the transmission coefficient itself can have strong frequency dependence, in which case the frequency dependence of the scattering rate would be stronger than the linear dependence assumed in the work. To proceed, we fit the thermal conductivity data using the $\sim \omega^0$, $\sim \omega^1$, $\sim \omega^2$ frequency dependencies respectively in the grain boundary scattering rate discussed above.

5.4.4 Thermal conductivity modeling

To obtain the fit, we follow an approach to modeling thermal conductivity similar to those proposed by Callaway¹²⁶ and Holland¹²⁷ but include a modification proposed by Mingo¹²¹. Mingo suggests the use of a cut off frequency, ω_c smaller than the Debye frequency, ω_D in fitting the experimental thermal conductivity of silicon nanostructures. This approach accounts for the difference in the phonon dispersion relation between the Holland model and more accurate lattice dynamics calculations. Here, we follow Mingo's approach and treat ω_c as a fitting parameter in subsequent modeling. We note that the fit is not overly sensitive to the particular value of ω_c since Umklapp scattering strongly reduces the contribution of high frequency phonons to heat conduction much before the cut-off frequency¹²⁸.

Assuming a linear dispersion relation and treating all polarizations equivalently, the expression for thermal conductivity is

$$\kappa = \frac{1}{2\pi^2 k_B T^2 v} \int_0^{\omega_c} \frac{(\hbar\omega)^2 \omega^2 e^{\hbar\omega/k_B T}}{[e^{\hbar\omega/k_B T} - 1]^2} \tau(\omega) d\omega \quad (6)$$

where $v = 6.4 \times 10^3$ m/s is now the average phonon propagation speed¹²⁷, k_B is the Boltzmann constant and \hbar is the reduced Planck's constant. The frequency dependent phonon relaxation time $\tau(\omega)$ can be calculated using Matthiessen's rule, assuming scattering due to isotopes, Umklapp processes, surfaces and grain boundaries to be independent. We use scattering rates from the literature^{126,129} for mass difference (isotope) and Umklapp scattering. These are of the form $\tau_m^{-1} = A\omega^4$ and $\tau_u^{-1} = BT\omega^2 e^{-C/T}$. The value of A depends on the isotope concentration and we assume the commonly used value¹²⁷, $A = 1.32 \times 10^{-45}$ s³. We follow Ref. ¹²⁸ in determining the values of B , C and ω_c . This approach yields fits to the high temperature thermal

conductivities of bulk silicon and inverse opals using identical values of the parameters, $B=1.6\times 10^{19}$ s/K, $C=152$ K and $\omega_c=4.3\times 10^{13}$ rad/s. We note that the cut-off frequency obtained here compares well with Mingo's fits to single crystal nanowires, which yields 4.2×10^{13} rad/s.

Surface scattering in an inverse opal is complicated due to the complex geometry. A rigorous but tedious approach involves solving the phonon Boltzmann equation in the exact geometry. However, the main effect of the lattice geometry is the macroscopic bending of heat flux lines rather than microscopic effects on phonon transport, due to the relatively large curvatures involved. Further, grain boundaries likely randomize phonon scattering and remove any geometrical effect of the lattice in surface scattering. With this in mind, we adopt a simpler approach in modeling surface scattering. We assume scattering from the surfaces of the thin segments of the inverse opal to be the same as scattering from the surface of a thin film. Using Casimir's approach, we obtain $\tau_b^{-1} = v/(Fd)$ where $F=4$ for a thin-film geometry¹³⁰. We show below that this approach leads to excellent fits for all samples, validating our simplifying assumptions.

5.5 Results and discussion

Figure 5.6 plots the scattering rates obtained from best fits to the data. Surface scattering appears as a flat line in the Casimir approximation and is based on the shell thickness as the feature size. Since the grain size in these samples is approximately equal to the shell thickness, the surface scattering rate is approximately the same as that for frequency independent grain boundary scattering. Overall, surface scattering dominates at low frequencies and grain boundary

scattering dominates at higher frequencies. The contribution from grain boundary scattering is always significant except for very low frequencies that contribute little to heat conduction across the temperature range of the data. The previously suggested $\sim\omega^1$ model and the coherent $\sim\omega^2$ models yield rates larger than surface scattering, for phonon frequencies exceeding ~ 1 THz. The $\sim\omega^2$ rate diverges from the $\sim\omega^1$ rate at frequencies lower than ~ 1.5 THz and is approximately one order of magnitude smaller at the lowest frequencies. We note that Umklapp scattering rates are more than an order of magnitude smaller than the dominant rates, even at 300 K. Overall, these calculations suggest that the contribution of a frequency dependent grain boundary scattering alters the temperature dependence of the thermal conductivity data from the $\sim T^3$ dependence when lower phonon frequencies dominate heat conduction. The frequency dependence is insignificant when the higher frequency part of the spectrum in **Figure 5.6** dominates heat conduction, such as at room temperatures.

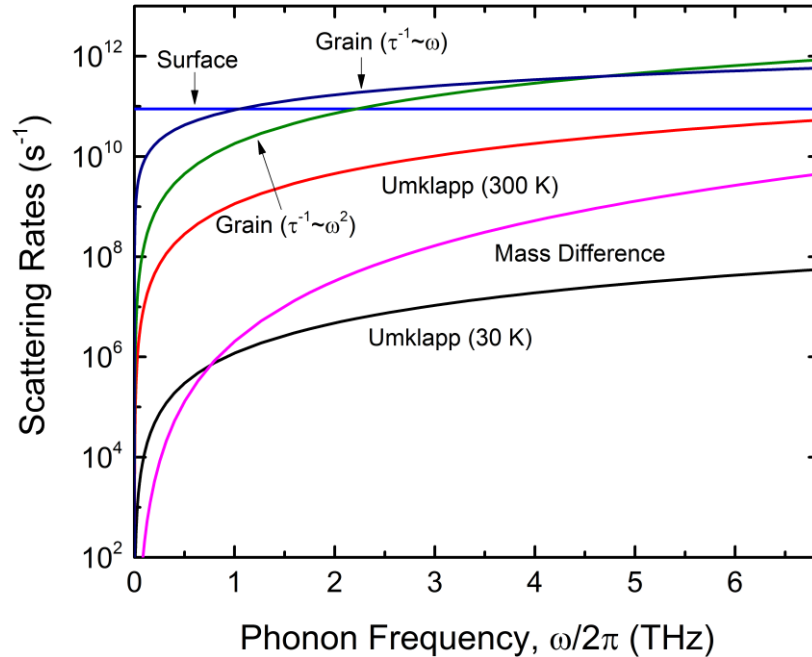


Figure 5.6 – Frequency dependent phonon scattering rates calculated for the inverse opal with smallest features ($d=18$ nm, $l=20$ nm). Rates for Umklapp scattering are shown at 30 K and 300 K. The deviation between two grain boundary scattering models becomes significant at frequencies below 2 THz.

Referring back to **Figure 5.5**, all three models for grain boundary scattering fit the data reasonably well at temperature above 200 K. **Figure 5.5** only shows the fit obtained using the $\sim \omega^2$ frequency dependent model but the $\sim \omega^0$, $\sim \omega^1$ models fit the data equally well near room temperature. However, the low temperature behavior is significantly different. **Figure 5.7** shows the low temperature data with error bars and includes the best fits from the $\sim \omega^0$, $\sim \omega^1$, $\sim \omega^2$ scattering rates. We find that only the $\sim \omega^2$ dependent rate corresponding to coherent scattering in the inter-grain region, is able to fit the data reasonably well at the lowest temperatures. There is a systematic trend in the agreement of the other models with the data. Predictions from the frequency independent model increasingly diverge from the data below temperatures of ~ 200 K whereas predictions from the $\sim \omega^1$ model increasingly diverge from the data below ~ 140 K. Only the $\sim \omega^2$ model fits the data down to 30 K. Further, the values of the inter-grain thickness obtained from the best fits range between 1.8-2.2 Å, consistent with values calculated using molecular dynamics of bulk silicon for grain boundaries of different energies^{125,131}. In fact, the frequency dependence of the phonon reflection coefficient calculated from these simulations follows $\sim \omega^{2.3-2.5}$, approximately consistent with the proposed model. The excellent agreement of the data with the coherent model and the agreement of the frequency dependency in the model with atomistic calculations, strongly suggest that grain boundary scattering is indeed coherent in silicon inverse opals at low temperatures. The reason behind this is not clear at present. An obvious hypothesis is that grain boundaries in silicon inverse opals possess relatively lower disorder and/or are thinner compared to bulk or thin film polysilicon. In either case, this enables coherence in phonon reflections from the inter-grain region at low temperatures.

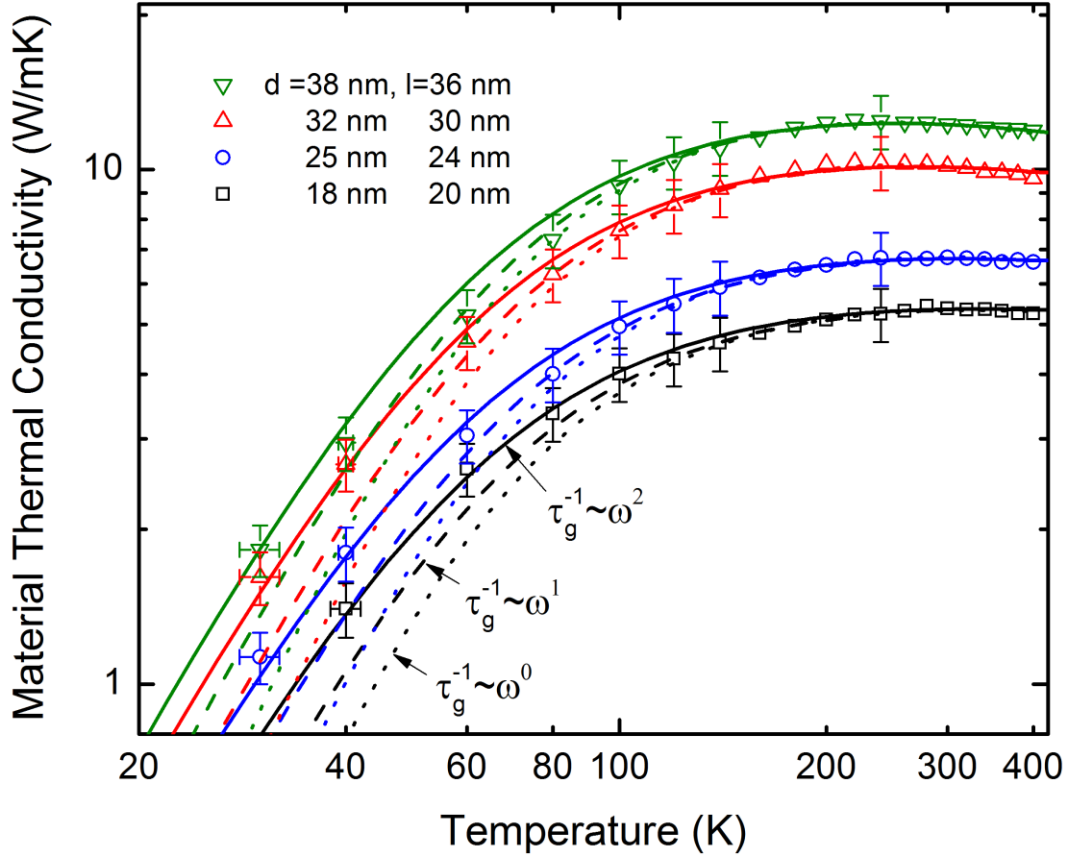


Figure 5.7 – The material thermal conductivities of inverse opals vary as $\sim T^{1.8}$ at low temperatures. Quadratic frequency dependence in the phonon grain boundary scattering rate yields excellent agreement with data. The solid curves use $\sim \omega^2$ dependent grain boundary scattering rate while the dashed and dotted curves use $\sim \omega^1$ and $\sim \omega^0$ dependent rates. The $\sim \omega^2$ dependence arises due to coherent scattering in the inter-grain region.

5.6 Conclusion

In conclusion, thermal conductivity measurements on silicon inverse opals show effective thermal conductivities $\lesssim 1$ W/mK and material thermal conductivities $\lesssim 10$ W/mK at room temperature. The relatively low thermal conductivities are significant in photonic applications where even relatively small absorption can cause significant temperature rise. In exploring phonon transport in these structures, we find that frequency-dependent, coherent phonon grain

boundary scattering explains the data across the temperature range of the measurement down to 30 K. Compared to previous measurements, inverse opals provide access to more uniform grains across the entire sample since grain growth is restricted by the thickness of the silicon shell. Based on the thermal conductivity analysis, we hypothesize that the inter-grain region is thinner and possesses lesser disorder than typical polysilicon films. This is likely the reason for the clear frequency dependence in our data at low temperatures that is not observed in previous measurements. Assuming that inverse opals can be heavily doped similar to bulk polysilicon, these materials become interesting for thermoelectric energy conversion at high temperatures. Theoretical calculations¹³² show $ZT \sim 0.6$ at 600 K, providing impetus for future experiments. This work provides thermal conductivity data useful in technological applications of inverse opals and insight into the physics of phonon heat conduction in these structures.

REFERENCES

- 1 Barnes, W. L., Dereux, A. & Ebbesen, T. W. Surface plasmon subwavelength optics. *Nature* 424, 824-830 (2003).
- 2 Gramotnev, D. K. & Bozhevolnyi, S. I. Plasmonics beyond the diffraction limit. *Nat Photonics* 4, 83-91, doi:DOI 10.1038/nphoton.2009.282 (2010).
- 3 Leonhardt, U. Optical metamaterials - Invisibility cup. *Nat Photonics* 1, 207-208, doi:DOI 10.1038/nphoton.2007.38 (2007).
- 4 Maier, S. A. *Plasmonics: Fundamentals and Applications*. (Springer, 2007).
- 5 Homola, J. *Surface Plasmon Resonance Based Sensors*. (Springer, 2006).
- 6 Raether, H. Surface-Plasmons on Smooth and Rough Surfaces and on Gratings. *Springer Tr Mod Phys* 111, 1-133 (1988).
- 7 Burstein, E., Chen, W. P., Chen, Y. J. & Hartstein, A. Surface Polaritons - Propagating Electromagnetic Modes at Interfaces. *J Vac Sci Technol* 11, 1004-1019, doi:DOI 10.1116/1.1318673 (1974).
- 8 Willets, K. A. & Van Duyne, R. P. Localized surface plasmon resonance spectroscopy and sensing. *Annu Rev Phys Chem* 58, 267-297, doi:DOI 10.1146/annurev.physchem.58.032806.104607 (2007).
- 9 Wood, R. M. On a remarkable case of uneven distribution of light in a diffraction grating spectrum. *Phil. Mag.* 4, 396-408 (1902).
- 10 Garnett, J. C. M. Colours in Metal Glasses and in Metallic Films. *Philosophical Transactions of the Royal Society of London. Series A, Containing Papers of a Mathematical or Physical Character* 203, 385-420, doi:10.1098/rsta.1904.0024 (1904).
- 11 Rayleigh, L. *Phil. Mag.* 4, 375 (1899).
- 12 Mie, G. Beiträge zur Optik trüber Medien, speziell kolloidaler Metallösungen. *Ann. Phys. (Leipzig)* 25, 377-445 (1908).
- 13 Ritchie, R. H. Plasma Losses by Fast Electrons in Thin Films. *Physical Review* 106, 874-881 (1957).
- 14 Ritchie, R. H., Arakawa, E. T., Cowan, J. J. & Hamm, R. N. Surface-Plasmon Resonance Effect in Grating Diffraction. *Physical Review Letters* 21, 1530-1533 (1968).
- 15 Otto, A. Excitation of nonradiative surface plasma waves in silver by the method of frustrated total refraction. *Z. Phys.* 216, 398-410 (1968).
- 16 Kretschm, E. & Raether, H. Radiative Decay of Non Radiative Surface Plasmons Excited by Light. *Z Naturforsch Pt A A* 23, 2135-& (1968).
- 17 Cunningham, S. L., Maradudin, A. A. & Wallis, R. F. Effect of a charge layer on the surface-plasmon-polariton dispersion curve. *Physical Review B* 10, 3342-3355 (1974).

- 18 Smith, D. R., Pendry, J. B. & Wiltshire, M. C. K. Metamaterials and negative refractive index. *Science* 305, 788-792 (2004).
- 19 Quinten, M., Leitner, A., Krenn, J. R. & Aussenegg, F. R. Electromagnetic energy transport via linear chains of silver nanoparticles. *Opt. Lett.* 23, 1331-1333 (1998).
- 20 Oulton, R. F., Sorger, V. J., Genov, D. A., Pile, D. F. P. & Zhang, X. A hybrid plasmonic waveguide for subwavelength confinement and long-range propagation. *Nat Photonics* 2, 496-500 (2008).
- 21 Maier, S. A., Kik, P. G., Atwater, H. A., Meltzer, S., Harel, E., Koel, B. E. & Requicha, A. A. G. Local detection of electromagnetic energy transport below the diffraction limit in metal nanoparticle plasmon waveguides. *Nat Mater* 2, 229-232 (2003).
- 22 Bozhevolnyi, S. I., Erland, J., Leosson, K., Skovgaard, P. M. W. & Hvam, J. M. Waveguiding in Surface Plasmon Polariton Band Gap Structures. *Physical Review Letters* 86, 3008-3011 (2001).
- 23 Lu, Y., Liu, G. L., Kim, J., Mejia, Y. X. & Lee, L. P. Nanophotonic Crescent Moon Structures with Sharp Edge for Ultrasensitive Biomolecular Detection by Local Electromagnetic Field Enhancement Effect. *Nano Letters* 5, 119-124, doi:10.1021/nl048232+ (2004).
- 24 Green, R. J., Frazier, R. A., Shakesheff, K. M., Davies, M. C., Roberts, C. J. & Tendler, S. J. B. Surface plasmon resonance analysis of dynamic biological interactions with biomaterials. *Biomaterials* 21, 1823-1835 (2000).
- 25 Anker, J. N., Hall, W. P., Lyandres, O., Shah, N. C., Zhao, J. & Duyne, P. V. Biosensing with plasmonic nanosensors. *Nat Mater* 7, 442-453 (2008).
- 26 Shao, D. B. & Chen, S. C. Surface-plasmon-assisted nanoscale photolithography by polarized light. *Applied Physics Letters* 86, 253107-253103 (2005).
- 27 Lezec, H. & Thio, T. Diffracted evanescent wave model for enhanced and suppressed optical transmission through subwavelength hole arrays. *Opt. Express* 12, 3629-3651 (2004).
- 28 Kim, Y. K., Lundquist, P. M., Helfrich, J. A., Mikrut, J. M., Auvin, P. R. & Ketterson, J. B. Scanning plasmon optical microscope. *Applied Physics Letters* 66, 3407-3409 (1995).
- 29 Fang, Y., Seong, N.-H. & Dlott, D. D. Measurement of the Distribution of Site Enhancements in Surface-Enhanced Raman Scattering. *Science* 321, 388-392, doi:10.1126/science.1159499 (2008).
- 30 Fang, N., Lee, H., Sun, C. & Zhang, X. Sub-Diffraction-Limited Optical Imaging with a Silver Superlens. *Science* 308, 534-537, doi:10.1126/science.1108759 (2005).
- 31 Stenzel, O., Stendal, A., Voigtsberger, K. & von Borczyskowski, C. Enhancement of the photovoltaic conversion efficiency of copper phthalocyanine thin film devices by incorporation of metal clusters. *Solar Energy Materials and Solar Cells* 37, 337-348, doi:10.1016/0927-0248(95)00027-5 (1995).

- 32 Ferry, V. E., Sweatlock, L. A., Pacifici, D. & Atwater, H. A. Plasmonic Nanostructure Design for Efficient Light Coupling into Solar Cells. *Nano Letters* 8, 4391-4397, doi:10.1021/nl8022548 (2008).
- 33 Radke, A., Gissibl, T., Klotzbücher, T., Braun, P. V. & Giessen, H. Three-Dimensional Bichiral Plasmonic Crystals Fabricated by Direct Laser Writing and Electroless Silver Plating. *Advanced Materials* 23, 3018-3021, doi:10.1002/adma.201100543 (2011).
- 34 Li, J., Hossain, M. D. M., Jia, B., Buso, D. & Gu, M. Three-dimensional hybrid photonic crystals merged with localized plasmon resonances. *Opt. Express* 18, 4491-4498 (2010).
- 35 Nikolajsen, T., Leosson, K. & Bozhevolnyi, S. I. Surface plasmon polariton based modulators and switches operating at telecom wavelengths. *Applied Physics Letters* 85, 5833-5835 (2004).
- 36 Schuller, J. A., Barnard, E. S., Cai, W., Jun, Y. C., White, J. S. & Brongersma, L. Plasmonics for extreme light concentration and manipulation (vol 9, pg 193, 2010). *Nat Mater* 9 (2010).
- 37 Miyazaki, H. T. & Kurokawa, Y. Squeezing Visible Light Waves into a 3-nm-Thick and 55-nm-Long Plasmon Cavity. *Physical Review Letters* 96, 097401 (2006).
- 38 Shalaev, V. M. Optical negative-index metamaterials. *Nat Photonics* 1, 41-48 (2007).
- 39 Smith, D. R., Padilla, W. J., Vier, D. C., Nemat-Nasser, S. C. & Schultz, S. Composite medium with simultaneously negative permeability and permittivity. *Phys Rev Lett* 84, 4184-4187 (2000).
- 40 John, S. Strong Localization of Photons in Certain Disordered Dielectric Superlattices. *Phys Rev Lett* 58, 2486-2489 (1987).
- 41 Russell, P. S. J. Photonic crystals: Molding the flow of light - Joannopoulos, J. D., Meade, R. D., Winn, J. N. *Nature* 381, 290-290 (1996).
- 42 Yablonovitch, E. Photonic crystals: Semiconductors of light. *Sci Am* 285, 46-+ (2001).
- 43 Yariv, A., Xu, Y., Lee, R. K. & Scherer, A. Coupled-resonator optical waveguide: a proposal and analysis. *Opt Lett* 24, 711-713 (1999).
- 44 Feigenbaum, E. & Atwater, H. A. Resonant Guided Wave Networks. *Phys Rev Lett* 104 (2010).
- 45 Feigenbaum, E., Burgos, S. P. & Atwater, H. A. Programming of inhomogeneous resonant guided wave networks. *Opt Express* 18, 25584-25595 (2010).
- 46 Feigenbaum, E. & Orenstein, M. Perfect 4-way splitting in nano plasmonic X-junctions. *Opt Express* 15, 17948-17953 (2007).
- 47 Gratson, G. M., Garcia-Santamaria, F., Lousse, V., Xu, M., Fan, S., Lewis, J. A. & Braun, P. V. Direct-write assembly of three-dimensional photonic crystals: Conversion of polymer scaffolds to silicon hollow-woodpile structures. *Adv Mater* 18, 461-+ (2006).
- 48 Joannopoulos, J. D., Villeneuve, P. R. & Fan, S. H. Photonic crystals: Putting a new twist on light. *Nature* 386, 143-149 (1997).

- 49 Therriault, D., White, S. R. & Lewis, J. A. Chaotic mixing in three-dimensional microvascular networks fabricated by direct-write assembly. *Nat Mater* 2, 265-271 (2003).
- 50 Spearing, S. M. Materials issues in microelectromechanical systems (MEMS). *Acta Mater* 48, 179-196 (2000).
- 51 Li, Y. Y., Cunin, F., Link, J. R., Gao, T., Betts, R. E., Reiver, S. H., Chin, V., Bhatia, S. N. & Sailor M. J. Polymer replicas of photonic porous silicon for sensing and drug delivery applications. *Science* 299, 2045-2047 (2003).
- 52 LaVan, D. A., McGuire, T. & Langer, R. Small-scale systems for in vivo drug delivery. *Nat Biotechnol* 21, 1184-1191 (2003).
- 53 Hu, L. B., Choi, J. W., Yang, Y., Jeong, Sangmoo, Mantia, F. L., Cui, L., & Cui, Y. Highly conductive paper for energy-storage devices. *P Natl Acad Sci USA* 106, 21490-21494 (2009).
- 54 Arpin, K. A., Mihi, A., Johnson, H. T., Baca, A. J., Rogers, J. A., Lewis, J. A. & Braun, P. V. Multidimensional Architectures for Functional Optical Devices. *Adv Mater* 22, 1084-1101 (2010).
- 55 Lewis, J. A. Direct ink writing of 3D functional materials. *Adv Funct Mater* 16, 2193-2204 (2006).
- 56 Ahn, B. Y., Lorang, D. J. & Lewis, J. A. Transparent conductive grids via direct writing of silver nanoparticle inks. *Nanoscale* 3, 2700-2702 (2011).
- 57 Johnson, P. B. & Christy, R. W. Optical Constants of Noble Metals. *Phys Rev B* 6, 4370-4379 (1972).
- 58 Atwater, H. A. & Polman, A. Plasmonics for improved photovoltaic devices (vol 9, pg 205, 2010). *Nat Mater* 9, 865-865 (2010).
- 59 Tegtart, W. J., The Electrolytic and Chemical Polishing of Metals, Pergamon Press Ltd. P. 68 (1959)
- 60 Kay, D., Techniques for Electron Microscopy, Alden Press Ltd., p. 403 (1965).
- 61 Lyles, R., Rothman, S. & Jäger, W. A cyanide-free solution for electropolishing silver. *Metallography* 11, 361-363 (1978).
- 62 Groenewald, T. Potential applications of thiourea in the processing of gold. *Journal of the South African Institute of Mining and Metallurgy* 77, 217-223 (1977).
- 63 Jones, T. Electropolishing of precious metals. *Metal Finishing* 102, 45-57 (2004).
- 64 Nagpal, P., Lindquist, N. C., Oh, S. H. & Norris, D. J. Ultrasoother Patterned Metals for Plasmonics and Metamaterials. *Science* 325, 594-597 (2009).
- 65 Garcia-Santamaria, F., Ibisate, M., Rodriguez, I., Meseguer, F. & Lopez, C. Photonic band engineering in opals by growth of Si/Ge multilayer shells. *Adv Mater* 15, 788-+ (2003).
- 66 Vlasov, Y. A., Bo, X. Z., Sturm, J. C. & Norris, D. J. On-chip natural assembly of silicon photonic bandgap crystals. *Nature* 414, 289-293 (2001).

- 67 Terzaki, K., Vasilantonakis, N., Gaidukeviciute, A., Reinhardt, C., Fotakis, C., Vamvakaki, M. & Farsari, M. *et al.* 3 D conducting nanostructures fabricated using direct laser writing. *Optical Materials Express* 1, 586-597 (2011).
- 68 Radke, A., Gissibl, T., Klotzbücher, T., Braun, P. V. & Giessen, H. Three-dimensional bichiral plasmonic crystals fabricated by direct laser writing and electroless silver plating. *Adv Mater* 23, 3018-3021 (2011).
- 69 YUANJUN, Y. Fabrication of 3D metamaterials using two-photon polymerization and selective silver electroless plating. (2011).
- 70 Zalkovskij, M., Malureanu, R., Andryieuski, A. & Lavrinenko, A. in *SPIE Optics+ Optoelectronics*. 80700M-80700M-80707 (International Society for Optics and Photonics).
- 71 Astratov, V., Whittaker, D. M., Culshaw, I. S., Stevenson, R. M., Skolnick, M. S., Krauss, T. F. & De La Rue, R. M. Photonic band-structure effects in the reflectivity of periodically patterned waveguides. *Phys Rev B* 60, R16255 (1999).
- 72 Andreani, L., Balestreri, A., Galisteo-Lopez, J. F., Galli, M., Patrini, M., Descrovi, E., Chiodini, A., Giorgis, F., Pallavidino, L. & Geobaldo, F. Optical response with threefold symmetry axis on oriented microdomains of opal photonic crystals. *Phys Rev B* 78, 205304 (2008).
- 73 Billaudeau, C., Collin, S., Sauvan, C., Bardou, N., Pardo, F. & Pelouard, J. Angle-resolved transmission measurements through anisotropic two-dimensional plasmonic crystals. *Opt Lett* 33, 165-167 (2008).
- 74 Li, J., Jia, B., Zhou, G. & Gu, M. Fabrication of three-dimensional woodpile photonic crystals in a PbSe quantum dot composite material. *Opt. Express* 14, 10740-10745 (2006).
- 75 Tan, D., Li, Y., Qi, F., Yang, H., Gong, Q., Dong, X. & Duan, X. Reduction in feature size of two-photon polymerization using SCR500. *Applied physics letters* 90, 071106-071106-071103 (2007).
- 76 Pitts, J. D., Campagnola, P. J., Epling, G. A. & Goodman, S. L. Submicron multiphoton free-form fabrication of proteins and polymers: studies of reaction efficiencies and applications in sustained release. *Macromolecules* 33, 1514-1523 (2000).
- 77 Maruo, S., Ikuta, K. & Korogi, H. Submicron manipulation tools driven by light in a liquid. *Applied Physics Letters* 82, 133-135 (2003).
- 78 Ma, J., Parajuli, B. R., Ghossoub, M. C., Mihi, A., Sadhu, J., Braun, P. V. & Sinha, S. Coherent Phonon-Grain Boundary Scattering in Silicon Inverse Opals. *Nano Lett* 13, 618-624 (2013).
- 79 Majumdar, A. Thermoelectricity in Semiconductor Nanostructures. *Science* 303, 777-778, doi:10.1126/science.1093164 (2004).
- 80 Shakouri, A. Recent Developments in Semiconductor Thermoelectric Physics and Materials. *Annual Review of Materials Research* 41, 399-431, doi:doi:10.1146/annurev-matsci-062910-100445 (2011).

- 81 Nolas, G. S., Poon, J. & Kanatzidis, M. Recent developments in bulk thermoelectric materials. *MRS bulletin* 31, 199-205 (2006).
- 82 Snyder, G. J. & Toberer, E. S. Complex thermoelectric materials. *Nat Mater* 7, 105-114 (2008).
- 83 Hochbaum, A. I., Chen, R., Delgado, R. D., Liang, W., Garnett, E. C., Najarian, M., Majumdar, A. & Yang, P. Enhanced thermoelectric performance of rough silicon nanowires. *Nature* 451, 163-167 (2008).
- 84 Boukai, A. I., Bunimovich, Y., Tahir-Kheli, J., Yu, J., Goddard III, W. A. & Heath, J. R. Silicon nanowires as efficient thermoelectric materials. *Nature* 451, 168-171 (2008).
- 85 Hopkins, P. E., Reinke, C. M., Su, M. F., Olsson, R. H., Shaner, E. A., Leseman, Z. C., Serrano, J. R., Phinney, L. M. & El-Kady, I. Reduction in the thermal conductivity of single crystalline silicon by phononic crystal patterning. *Nano Lett* 11, 107-112 (2010).
- 86 Norris, D. J., Arlinghaus, E. G., Meng, L., Heiny, R. & Scriven, L. E. Opaline Photonic Crystals: How Does Self-Assembly Work? *Advanced Materials* 16, 1393-1399, doi:10.1002/adma.200400455 (2004).
- 87 Meseguer, F., Blanco, A., Miguez, H., García-Santamaría, F., Ibasate, M. & Lopez, C. Synthesis of inverse opals. *Colloids and Surfaces A: Physicochemical and Engineering Aspects* 202, 281-290, doi:10.1016/S0927-7757(01)01084-6 (2002).
- 88 Tétreault, N., Míguez, H. & Ozin, G. A. Silicon Inverse Opal—A Platform for Photonic Bandgap Research. *Advanced Materials* 16, 1471-1476, doi:10.1002/adma.200400618 (2004).
- 89 Braun, P. V., Rinne, S. A. & García-Santamaría, F. Introducing Defects in 3D Photonic Crystals: State of the Art. *Advanced Materials* 18, 2665-2678, doi:10.1002/adma.200600769 (2006).
- 90 Blanco, A. *et al.* Large-scale synthesis of a silicon photonic crystal with a complete three-dimensional bandgap near 1.5 micrometres. *Nature* 405, 437-440 (2000).
- 91 Lee, J.-H., Galli, G. A. & Grossman, J. C. Nanoporous Si as an Efficient Thermoelectric Material. *Nano Letters* 8, 3750-3754, doi:10.1021/nl802045f (2008).
- 92 Yu, J.-K., Mitrovic, S., Tham, D., Varghese, J. & Heath, J. R. Reduction of thermal conductivity in phononic nanomesh structures. *Nat Nano* 5, 718-721, doi:http://www.nature.com/nnano/journal/v5/n10/abs/nnano.2010.149.html#supplementary-information (2010).
- 93 Tang, J., Wang, H., Lee, D. H., Fardy, M., Huo, Z., Russell, T. P. & Yang, P. Holey Silicon as an Efficient Thermoelectric Material. *Nano Letters* 10, 4279-4283, doi:10.1021/nl102931z (2010).
- 94 Chen, J., Zhang, G. & Li, B. Phonon coherent resonance and its effect on thermal transport in core-shell nanowires. *The Journal of Chemical Physics* 135, 104508-104508 (2011).

- 95 Wingert, M. C., Chen, Z. C., Dechaumphai, E., Moon, J., Xiang, J. & Chen, R. Thermal Conductivity of Ge and Ge–Si Core–Shell Nanowires in the Phonon Confinement Regime. *Nano Letters* 11, 5507-5513, doi:10.1021/nl203356h (2011).
- 96 Chen, J., Zhang, G. & Li, B. Impacts of Atomistic Coating on Thermal Conductivity of Germanium Nanowires. *Nano Letters* 12, 2826-2832, doi:10.1021/nl300208c (2012).
- 97 Albrecht, J. D., Knipp, P. A. & Reinecke, T. L. Thermal conductivity of opals and related composites. *Physical Review B* 63, 134303 (2001).
- 98 Maxwell, J. C. *A Treatise on Electricity and Magnetism*. (Oxford : Clarendon Press, 1873).
- 99 Kushwaha, M. S., Halevi, P., Dobrzynski, L. & Djafari-Rouhani, B. Acoustic band structure of periodic elastic composites. *Physical Review Letters* 71, 2022-2025 (1993).
- 100 Liu, Z., Zhang, X., Mao, Y., Zhu, Y. Y., Yang, Z., Chan, C. T. & Sheng P. Locally Resonant Sonic Materials. *Science* 289, 1734-1736, doi:10.1126/science.289.5485.1734 (2000).
- 101 McConnell, A. D. & Goodson, K. E. THERMAL CONDUCTION IN SILICON MICRO-AND NANOSTRUCTURES. *Annual Review of Heat Transfer* 14, 129-168 (2005).
- 102 Wang, Z., Alaniz, J. E., Jang, W., Garay, J. E. & Dames, C. Thermal Conductivity of Nanocrystalline Silicon: Importance of Grain Size and Frequency-Dependent Mean Free Paths. *Nano Letters* 11, 2206-2213, doi:10.1021/nl1045395 (2011).
- 103 Vlasov, Y. A., Bo, X.-Z., Sturm, J. C. & Norris, D. J. On-chip natural assembly of silicon photonic bandgap crystals. *Nature* 414, 289-293 (2001).
- 104 Stöber, W., Fink, A. & Bohn, E. Controlled growth of monodisperse silica spheres in the micron size range. *Journal of Colloid and Interface Science* 26, 62-69, doi:10.1016/0021-9797(68)90272-5 (1968).
- 105 Chabanov, A. A., Jun, Y. & Norris, D. J. Avoiding cracks in self-assembled photonic band-gap crystals. *Applied Physics Letters* 84, 3573-3575 (2004).
- 106 Jiang, P., Bertone, J. F., Hwang, K. S. & Colvin, V. L. Single-crystal colloidal multilayers of controlled thickness. *Chem Mater* 11, 2132-2140 (1999).
- 107 García-Santamaría, F., Nelson, E. C. & Braun, P. V. Optical surface resonance may render photonic crystals ineffective. *Physical Review B* 76, 075132 (2007).
- 108 The corresponding porosity of the inverse opal structure is $1-86\%*(1-0.74)=78\%$
- 109 King, J. S., Graugnard, E. & Summers, C. J. TiO₂ Inverse Opals Fabricated Using Low-Temperature Atomic Layer Deposition. *Advanced Materials* 17, 1010-1013, doi:10.1002/adma.200400648 (2005).
- 110 Beck, P. A. S., P.R. *Trans. AIME* 180, 240 (1949).
- 111 Cahill, D. G. Thermal conductivity measurement from 30 to 750 K: the 3 omega method. *Review of Scientific Instruments* 61, 802-808 (1990).
- 112 Cahill, D. G., Katiyar, M. & Abelson, J. R. Thermal conductivity of a-Si:H thin films. *Physical Review B* 50, 6077-6081 (1994).

- 113 Dames, C. & Chen, G. 1 omega, 2 omega, and 3 omega methods for measurements of thermal properties. *Review of Scientific Instruments* 76, 124902-124914 (2005).
- 114 Borca-Tasciuc, T., Kumar, A. R. & Chen, G. Data reduction in 3 omega method for thin-film thermal conductivity determination. *Rev Sci Instrum* 72, 2139-2147 (2001).
- 115 Asheghi, M., Leung, Y. K., Wong, S. S. & Goodson, K. E. Phonon-boundary scattering in thin silicon layers. *Appl Phys Lett* 71, 1798-1800 (1997).
- 116 Uma, S., McConnell, A. D., Asheghi, M., Kurabayashi, K. & Goodson, K. E. Temperature-dependent thermal conductivity of undoped polycrystalline silicon layers. *Int J Thermophys* 22, 605-616 (2001).
- 117 Lee, S. M. & Cahill, D. G. Heat transport in thin dielectric films. *Journal of Applied Physics* 81, 2590-2595 (1997).
- 118 Bid, A., Bora, A. & Raychaudhuri, A. K. Temperature dependence of the resistance of metallic nanowires of diameter $\geq 15\text{nm}$: Applicability of Bloch-Grüneisen theorem. *Physical Review B* 74, 035426 (2006).
- 119 After fabrication, each sample was cleaved into two pieces: one for XRD and one for thermal measurement.
- 120 Klemens, P. G. Heat conduction in solids by phonons. *Thermochimica Acta* 218, 247-255, doi:10.1016/0040-6031(93)80426-B (1993).
- 121 Mingo, N. Calculation of Si nanowire thermal conductivity using complete phonon dispersion relations. *Physical Review B* 68, 113308 (2003).
- 122 Casimir, H. B. G. Note on the conduction of heat in crystals. *Physica* 5, 495-500, doi:10.1016/S0031-8914(38)80162-2 (1938).
- 123 Sadhu, J. & Sinha, S. Room-temperature phonon boundary scattering below the Casimir limit. *Physical Review B* 84, 115450 (2011).
- 124 Klemens, P. G. Phonon scattering and thermal resistance due to grain boundaries. *International Journal of Thermophysics* 15, 1345-1351, doi:10.1007/BF01458842 (1994).
- 125 Schelling, P. K., Phillpot, S. R. & Keblinski, P. Kapitza conductance and phonon scattering at grain boundaries by simulation. *Journal of Applied Physics* 95, 6082-6091 (2004).
- 126 Callaway, J. Model for Lattice Thermal Conductivity at Low Temperatures. *Physical Review* 113, 1046-1051 (1959).
- 127 Holland, M. G. Analysis of Lattice Thermal Conductivity. *Phys Rev* 132, 2461-& (1963).
- 128 Li, D. *Thermal Transport in Individual Nanowires and Nanotubes* Doctor of Philosophy thesis, UNIVERSITY OF CALIFORNIA, BERKELEY, (2002).
- 129 Asen-Palmer, M. *et al.* Thermal conductivity of germanium crystals with different isotopic compositions. *Physical Review B* 56, 9431-9447 (1997).
- 130 Wang, Z. & Mingo, N. Absence of Casimir regime in two-dimensional nanoribbon phonon conduction. *Applied Physics Letters* 99, 101903-101903 (2011).

- 131 Keglinski, P., Phillpot, S. R., Wolf, D. & Gleiter, H. On the Thermodynamic Stability of Amorphous Intergranular Films in Covalent Materials. *Journal of the American Ceramic Society* 80, 717-732, doi:10.1111/j.1151-2916.1997.tb02889.x (1997).
- 132 Ma, J. & Sinha, S. Thermoelectric properties of highly doped n-type polysilicon inverse opals. *Journal of Applied Physics* 112, 073719-073719 (2012).